



Soft Matter

Biofilms at interfaces: microbial distribution in floating films

Journal:	<i>Soft Matter</i>
Manuscript ID	SM-ART-10-2019-002038.R1
Article Type:	Paper
Date Submitted by the Author:	19-Dec-2019
Complete List of Authors:	Desai, Nikhil; Purdue University System, Ardekani, Arezoo; Purdue University System,

SCHOLARONE™
Manuscripts

Cite this: DOI: 00.0000/xxxxxxxxxx

Biofilms at interfaces: microbial distribution in floating films

Nikhil Desai and Arezoo M. Ardekani^a

Received Date

Accepted Date

DOI: 00.0000/xxxxxxxxxx

Cellular motility is a key function guiding microbial adhesion to interfaces, which is the first step in the formation of biofilms. The close association of biofilms and bioremediation has prompted extensive research aimed at comprehending the physics of microbial locomotion near interfaces. We study the dynamics and statistics of microorganisms in a ‘floating biofilm’, i.e., a confinement with an air-liquid interface on one side and a liquid-liquid interface on the other. We use a very general mathematical model, based on a multipole representation and probabilistic simulations, to ascertain the spatial distribution of microorganisms in films of different viscosities. Our results reveal that microorganisms can be distributed symmetrically or asymmetrically across the height of the film, depending on their morphology and the ratio of the film’s viscosity to that of the fluid substrate. Long-flagellated bacteria exhibit stable swimming parallel to the liquid-liquid interface when the bacterial film is less viscous than the underlying fluid. Bacteria with shorter flagella on the other hand, always swim away from the liquid-liquid interface and accumulate at the free surface. We also analyze microorganism dynamics in a flowing film and show how a microorganism’s ability to resist ‘flow-induced-erosion’ from interfaces is affected by its elongation and mode of propulsion. Our study generalizes past efforts on understanding microorganism dynamics under confinement by interfaces and provides key insights on biofilm initiation at liquid-liquid interfaces.

1 Introduction

Hydrodynamics of swimming microorganisms—a branch of physical sciences with ever-expanding frontiers—has seen intense research from a host of perspectives, an important one being the study of motility near rigid/fluid surfaces^{1–3}. The fluid flow around a microorganism swimming near a surface is fundamentally different than that in an unbounded domain. This difference stems from the fluid dynamic constraints (boundary conditions) imposed by ambient surfaces which result in a ‘hydrodynamic interaction’ of the microorganism with the surface. It can cause: (i) a change in the organism’s swimming speed, or, (ii) a change in its swimming trajectory due to an induced rotation, or, (iii) a drift toward the surface causing surface-accumulation. These physical effects have important consequences on the near-surface functions of microorganisms, e.g., navigation through confinements, foraging, host invasion, stress evasion, and nutrient-source-colonization^{4–6}. Knowledge of microbial locomotion near surfaces can thus drive discovery and inform developments in applications like mammalian fertilisation, control of infectious diseases, membrane anti-fouling and bacterial bioremediation.

In light of these motivations, a large number of analytical, numerical and experimental studies have been conducted on the motion of microorganisms near surfaces. These studies focus on the motion of micro-swimmers: (i) near a single rigid surface^{7–28}; (ii) near a single planar liquid-liquid interface^{27,29–33}; (iii) near a single deforming liquid-liquid interface^{34–36}; (iv) under confinement by two rigid surfaces^{37–41}; or, (v) under confinement by a rigid surface and a free surface (also called in a film)^{42,43}. Together, these investigations have revealed a fascinating array of swimming behavior displayed by micro-swimmers in the vicinity of surfaces. Motion near a single rigid/fluid surface has been categorized as: (i) attraction to rigid walls^{10,11,14,15,25,39}, (ii) attraction to non-deforming^{15,27,30,31} and deforming^{34,36} interfaces; (iii) swimming in circles with the directionality (clockwise vs. counter-clockwise when seen from the ‘microorganism side’) being determined by the rigidity/fluidity of the nearby surface^{8,21,27,32,33}; (iv) scattering away from a rigid wall^{14,28} or a free surface¹⁵; and, (v) swimming at a fixed distance from a nearby rigid surface^{11,16–19,27}, a plane, surfactant-laden free surface^{27,32,33} or deforming free surface³⁵. The swimming behavior within a fluid film is generally a combination of the above effects, depending on the swimmer’s proximity to either confining surface, and is useful in predicting microorganism distribu-

^aSchool of Mechanical Engineering, Purdue University, West Lafayette, IN, 47907, USA; E-mail: ardekani@purdue.edu

tion in biofilms^{42,43}. In addition, an imposed external flow can yield rich swimming dynamics of confined microorganisms, depending on the strength of the external flow and the swimmer-surface hydrodynamic interactions⁴⁴, e.g., (i) ‘trapping’ in high-shear regions^{45,46}, (ii) oscillating across the width of a parallel-plate channel^{47,48}, and, (iii) detachment of ‘hydrodynamically attached’ swimmers from a wall due to high external shear^{49,50}.

While hydrodynamics-mediated microbial distribution in biofilms resting on rigid substrates has received some attention^{42,43,50}, there are relatively fewer works which focus on *floating* biofilms. A floating biofilm is a unique configuration wherein microorganisms populate a fluid surface instead of a rigid one. It can be idealized as a suspension of microorganisms in a confinement with an air-liquid interface on one side and a liquid-liquid interface on the other. These systems, called “films of bacteria at interfaces”⁵¹, are becoming exceedingly relevant in applications like bioremediation of oil spills⁵², emulsion stabilization^{53,54}, pathogen control⁵⁵ and more fundamental processes like transfer of organic matter between the surface, the bulk and the substratum in lakes and oceans^{6,56}. Motivated by these applications, we wish to understand how hydrodynamics influences the distribution of microorganisms in floating films. Specifically, under what scenarios does hydrodynamics cause the microorganisms to preferentially reside at/near one of the two (air-liquid or liquid-liquid) confining interfaces? How is this preference affected if the film is flowing? The answer to these questions will depend on the microorganism’s geometry (shape and propulsion mechanism) and the physical properties of its surroundings (viscosities of its suspending and underlying fluids, external fluid-flow rates). Our aim is to develop a mathematical model that allows quantification of microorganism distribution across the height of the floating film, with consistent treatment of the flow-physics affecting microorganism dynamics. Towards this, we formulate a problem based on far-field hydrodynamics, stochastic simulation of microorganism trajectories and computation of their time-averaged spatial distributions. Section 2 introduces the mathematical model, followed by a description of the solution methodology employed. In Section 3.1 we describe the procedure used to obtain the main results in this manuscript, with Sections 3.2 and 3.3 discussing microbial dynamics in floating biofilms that are stagnant and flowing, respectively. Finally, Section 4 summarizes the main results, suggests many useful extensions of the present work and concludes this study.

2 Mathematical Model

The Reynolds number corresponding to microorganism swimming is small enough to neglect the effects of inertia on fluid flow and on the motion of the microorganism. The fluid flow is thus governed by the continuity and the Stokes flow equations. This also allows us to use a multipole expansion representation for the swimmer, i.e., we model the swimmer as a collection of Stokes flow singularities located at its centroid, and use them to evaluate any ensuing hydrodynamic interactions. The geometry of our problem is explained in Fig. 1. A microorganism of characteristic size a is contained in a fluid of viscosity μ_1 (henceforth called fluid-1), which floats on another fluid of viscosity μ_2 (fluid-2).

Any point of interest in the domain is identified by the coordinate $\mathbf{x} \equiv (x_1, x_2, x_3)$. The height of the fluid-1 film is H . The air-liquid (resp. liquid-liquid) interface at $x_3 = H$ (resp. $x_3 = 0$) is referred to as A-L (resp. L-L). The microbe’s configuration is uniquely identified by its height above the L-L, z , and its in-plane orientation, θ . We must note that the system described above is an idealization of a biofilm in that the fluid-1 is treated as a Newtonian fluid, and biofilms are generally complex structures characterized by a non-Newtonian environment. However, in this first exploration, we focus on films of bacteria in a Newtonian fluid, which is indeed an appropriate assumption in some instances^{6,57}. We emphasize that complex interfacial and bulk fluid behavior can be systematically incorporated into our mathematical model and comment further on this aspect in Section 4.

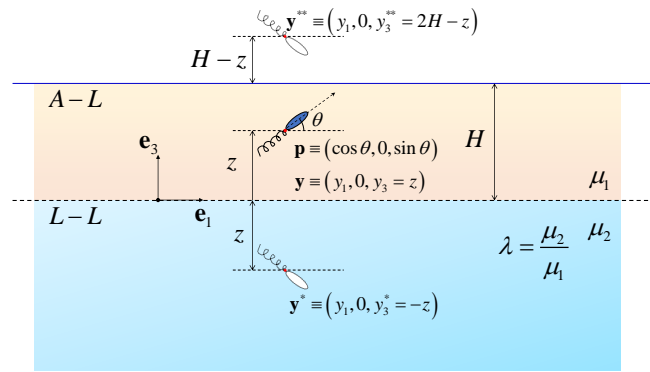


Fig. 1 A schematic of the problem being solved. Shown here is the microorganism located at $\mathbf{x} = \mathbf{y}$, along with its ‘images’ at \mathbf{y}^* (w.r.t. the liquid-liquid interface) and at \mathbf{y}^{**} (w.r.t. the air-liquid interface). A-L (resp. L-L) refers to the air-liquid (liquid-liquid) interface. Note that the \mathbf{e}_2 component of the swimmer’s orientation has been set to zero without loss of generality. The vertical distribution of a suspension of non-interacting microorganisms depends on the morphology of the microorganisms and the viscosity ratio, $\lambda \equiv \mu_2/\mu_1$, of the fluids involved.

2.1 Stokeslet in a floating film

We begin by describing the flow produced by a ‘point force singularity’ \mathbf{f} , also called a Stokeslet, acting at a position $\mathbf{x} = \mathbf{y}$ in fluid-1 in the floating film depicted in Fig. 1. Once the flow due to a Stokeslet is known, we can take its appropriate derivatives to construct the flow stemming from more complex force distributions characteristic of a swimming microorganism^{14,58}. The equations governing fluid flow in fluid-1 are:

$$\nabla \cdot \mathbf{u}^{(1)} = 0, \quad (1a)$$

$$-\nabla P^{(1)} + \mu_1 \nabla^2 \mathbf{u}^{(1)} + \mathbf{f} \delta(\mathbf{x} - \mathbf{y}) = \mathbf{0}, \quad (1b)$$

while those in fluid-2 are:

$$\nabla \cdot \mathbf{u}^{(2)} = 0, \quad (2a)$$

$$-\nabla P^{(2)} + \mu_2 \nabla^2 \mathbf{u}^{(2)} = \mathbf{0}, \quad (2b)$$

where, $P^{(i)}$, $\mathbf{u}^{(i)}$ and μ_i are the pressure, velocity and viscosity, respectively, in the i -th fluid. The fluid velocity fields $\mathbf{u}^{(1)}$ and

$\mathbf{u}^{(2)}$ must satisfy the continuity of velocity and shear stress at the liquid-liquid interface (L-L):

$$\mathbf{u}^{(1)} = \mathbf{u}^{(2)}, \text{ at } x_3 = 0, \quad (3a)$$

$$\mathbf{e}_3 \cdot \{\Delta \mathbf{T}\} \cdot \mathbf{e}_1 = \mathbf{e}_3 \cdot \{\Delta \mathbf{T}\} \cdot \mathbf{e}_2 = 0, \text{ at } x_3 = 0, \quad (3b)$$

where, $\mathbf{T}^{(i)} = -P^{(i)}\mathbf{I} + \mu_i(\nabla\mathbf{u}^{(i)} + \nabla\mathbf{u}^{(i),T})$ is the Newtonian stress tensor (\mathbf{I} is the identity tensor); and $\Delta\mathbf{T} = \mathbf{T}^{(1)} - \mathbf{T}^{(2)}$. In addition, the fluid velocity field $\mathbf{u}^{(1)}$ must satisfy the conditions of vanishing normal velocity and shear stress at the air-liquid interface (A-L):

$$\mathbf{e}_3 \cdot \mathbf{u}^{(1)} = 0, \text{ at } x_3 = H, \quad (4a)$$

$$\mathbf{e}_3 \cdot \mathbf{T}^{(1)} \cdot \mathbf{e}_1 = \mathbf{e}_3 \cdot \mathbf{T}^{(1)} \cdot \mathbf{e}_2 = 0, \text{ at } x_3 = H. \quad (4b)$$

The solution to eqns. 1 to 4 can be obtained by a methodology called the ‘method of images’, the details of which are given in the Appendix. If we treat the A-L and the L-L as plane mirrors, then we can identify ‘image points’ for the Stokeslet located at $\mathbf{x} = \mathbf{y}$. For example, the points \mathbf{y}^* and \mathbf{y}^{**} in Fig. 1 denote the images of the point \mathbf{y} with respect to the L-L and the A-L, respectively. Furthermore, \mathbf{y}^* (resp. \mathbf{y}^{**}) will also have an image with respect to the A-L (resp. the L-L) and in this way one can identify an infinite number of image positions^{42,59}. The fluid flow due to the confined Stokeslet is then represented by a superposition of the Stokeslet flow in an unbounded fluid, $\mathbf{u}_\infty^{(1)}(\mathbf{x})$, and the ‘film correction’, $\mathbf{u}^{\mathcal{H}}(\mathbf{x})$, due to systems of ‘image singularities’ located at the aforementioned image positions. Thus, we have:

$$\mathbf{u}^{(1)}(\mathbf{x}) = \mathbf{u}_\infty^{(1)}(\mathbf{x}) + \mathbf{u}^{\mathcal{H}}(\mathbf{x}), \quad (5)$$

with,

$$\mathbf{u}_\infty^{(1)}(\mathbf{x}) = \mathcal{G}^{Os}(\mathbf{x} - \mathbf{y}) \cdot \mathbf{f}, \quad (6)$$

where $\mathcal{G}^{Os}(\mathbf{x} - \mathbf{y})$ is called the Oseen tensor, and its tensorial expression is given in eqn. 27 in the Appendix. The film correction $\mathbf{u}^{\mathcal{H}}(\mathbf{x})$ is composed of flows due to image singularities, i.e., higher order flow singularities derived from the Stokeslet flow^{60–62}. In this work, we only obtain an approximate expression for $\mathbf{u}^{\mathcal{H}}(\mathbf{x})$, as we do not aim to ascertain the exact flow induced by the microorganism; rather, we are interested in studying the hydrodynamic interaction of the microorganism with the two interfaces. This interaction depends only on $\mathbf{u}^{\mathcal{H}}(\mathbf{x} = \mathbf{y})$, i.e., on the film correction evaluated at the position of the microorganism. The major contribution to this flow comes from the first two images: (i) the image at \mathbf{y}^* , taken with respect to the liquid-liquid interface (eqns. 28 and 29), and, (ii) the image at \mathbf{y}^{**} , taken with respect to the air-liquid interface (eqns. 31 and 32). Any higher order ‘image of image’ will always be further from the microorganism than the images at either \mathbf{y}^* or \mathbf{y}^{**} , so the dominant contribution to the hydrodynamic interactions will always stem from the two images shown in Fig. 1. This is especially true when considering thick fluid films, i.e., when $a/H \ll 1$. Therefore, we approximate the film correction, $\mathbf{u}^{\mathcal{H}}(\mathbf{x})$, as that due to the first two images of the Stokeslet:

$$\mathbf{u}^{\mathcal{H}}(\mathbf{x}) \approx \left[\mathcal{G}_1^{LL}(\mathbf{x}, \mathbf{y}, \mathbf{y}^*; \lambda) + \mathcal{G}_1^{AL}(\mathbf{x}, \mathbf{y}, \mathbf{y}^{**}) \right] \cdot \mathbf{f}, \quad (7)$$

where the tensorial expressions for \mathcal{G}_1^{LL} and \mathcal{G}_1^{AL} are given by eqns. 30 and 32 in the Appendix.

2.2 Higher order multipoles from the Stokeslet

Once the image system for a Stokeslet in a floating film is known (eqns. 7, 30 and 32), we can take its appropriate derivatives to construct the image systems for more complex force distributions. This is important because we are modeling the microorganism—and its hydrodynamic interactions with the interfaces—as a distribution of forces that its appendages exert on the fluid. These can be recovered by writing the multipole expansion form of the flow induced by the microorganism’s motion⁵⁸. For this, we assume the microorganism to be an axisymmetric prolate spheroid of major axis length $2a$ and minor axis length $2b$. At a given instant, it is located at $\mathbf{x} = \mathbf{y}$, and oriented along the direction \mathbf{p} . The multipole expansion of the flow due to the microorganism can be represented in terms of its contributions in an unbounded fluid, which involve gradients of the Oseen tensor $\mathcal{G}^{Os}(\mathbf{x} - \mathbf{y})$, plus correction terms—encoded in a tensor, say \mathcal{H} —stemming from the planar interfaces:

$$\mathbf{u}^{(1)}(\mathbf{x}) = \mathbf{u}^D(\mathbf{x}) + \mathbf{u}^{SD}(\mathbf{x}) + \mathbf{u}^Q(\mathbf{x}) + \mathbf{u}^R(\mathbf{x}) + \dots \quad (8)$$

The different terms in the right-hand side of eqn. 8 are given by:

$$\frac{\mathbf{u}^D}{8\pi\mu_1} = \kappa(\mathbf{p} \cdot \nabla_0) \left\{ \left(\mathcal{G}^{Os} + \mathcal{H} \right) \cdot \mathbf{p} \right\}, \quad (9a)$$

$$\frac{\mathbf{u}^{SD}}{8\pi\mu_1} = -\frac{\sigma}{2} \nabla_0^2 \left\{ \left(\mathcal{G}^{Os} + \mathcal{H} \right) \cdot \mathbf{p} \right\}, \quad (9b)$$

$$\frac{\mathbf{u}^Q}{8\pi\mu_1} = \nu(\mathbf{p}\mathbf{p} : \nabla_0 \nabla_0) \left\{ \left(\mathcal{G}^{Os} + \mathcal{H} \right) \cdot \mathbf{p} \right\}, \quad (9c)$$

$$\frac{\mathbf{u}^R}{8\pi\mu_1} = \tau(\mathbf{p} \cdot \nabla_0) \nabla_0 \times \left\{ \left(\mathcal{G}^{Os} + \mathcal{H} \right) \cdot \mathbf{p} \right\}, \quad (9d)$$

where, \mathcal{H} is approximated as:

$$\mathcal{H}(\mathbf{x}, \mathbf{y}, \mathbf{y}^*, \mathbf{y}^{**}; \lambda) \approx \mathcal{G}_1^{LL}(\mathbf{x}, \mathbf{y}, \mathbf{y}^*; \lambda) + \mathcal{G}_1^{AL}(\mathbf{x}, \mathbf{y}, \mathbf{y}^{**}). \quad (10)$$

Note that all directional gradients in eqn. 9 have been taken with respect to \mathbf{p} , which is a manifestation of the microorganism’s axisymmetry⁵⁸. The absence of any terms proportional to $\left(\mathcal{G}^{Os} + \mathcal{H} \right) \cdot \mathbf{p}$ signify that the microorganism does not exert any *net* force or torque on the fluid. The terms in eqns. 9a to 9d are collectively called the multipoles associated with the fluid flow generated by the microorganism. Specifically, they are termed the force dipole, the source dipole, the force quadrupole and the rotlet dipole respectively. The coefficients $\kappa, \sigma, \nu, \tau$ are called the strengths of each of these singularities. Dimensional consistency requires their dimensions to be: $[\kappa] = [\text{velocity} \times \text{length}^2]$ and $[\sigma, \nu, \tau] = [\text{velocity} \times \text{length}^3]$. Table 1 lists the signs of these coefficients for different microorganisms. These are estimated based on the physical meaning of each multipole and its relationship with the microorganism’s morphology, which we discuss next.

Each of the multipoles from eqn. 9 has a specific physical meaning. The force dipolar hydrodynamic interactions are the leading order effect of microbial swimming. Being force-free, a microorganism exerts equal and opposite forces on its surrounding fluid, which are represented by the force dipole. The sign of the dipole strength, κ , signifies two fundamentally distinct locomotion strategies. Microorganisms with $\kappa > 0$ are called ‘pushers’ because they *push* fluid *outward* along their bodies as they swim, e.g., *E. coli* and most flagellated bacteria. Exactly opposite to this, microorganisms with $\kappa < 0$ are called ‘pullers’ as they *pull* fluid *inward* along their bodies as they swim, e.g., the bi-flagellated alga *C. reinhardtii*, the uni-flagellated protozoan parasite *L. mexicana*. The pushing (resp. pulling) is achieved by locomotory appendages at the rear (resp. front) of the cell body¹. The dipole strength for pushers has been the most well studied multipole for swimming microorganisms^{22,39}. Its value can be estimated from the thrust force exerted by bacterial flagella, and it can range from 8 to 75 $\mu\text{m}^3/\text{s}$ based on various thrust force measurements^{22,39,63,64}. This range of values can also be obtained by noting that the force dipole coefficient scales as $\kappa \sim a^2 V_s$, where a is the characteristic size of the microorganism ($\approx 1 - 10 \mu\text{m}$), and V_s is its swimming speed ($\approx 10 - 100 \mu\text{m}/\text{s}$).

The source dipole represents the finite size of a microorganism. Source dipolar hydrodynamic interactions provide a finite size to the swimmer model by generating a separation of flow into regions inside and outside an impermeable boundary called the ‘hydrodynamic radius’ of the swimmer⁶⁵. The sign of the source dipole strength represents ciliated swimmers if $\sigma > 0$, and non-ciliated/flagellated swimmers if $\sigma < 0$ ^{14,42}. While the positive value of the source dipole strength for ciliated swimmers has indeed been measured for colonial *Volvox*⁶⁶, the same cannot be said for flagellated microorganisms. However, one can draw a comparison between a cell body ‘pushed’ by a flagellum and a sphere moving under an external force to estimate the sign of the source dipole for flagellated microorganisms^{14,42}. Therefore, since a sphere moving under an external force is represented by a Stokeslet and a negative source dipole, a force-free flagellated swimmer can be assumed to correspond to a negative source dipolar coefficient. The value of this coefficient can be estimated from the scaling $\sigma \sim -a^3 V_s$.

The force quadrupole represents the first effects of asymmetric forcing by the microorganism, stemming from an asymmetry in its shape. One of the primary sources of fore-aft asymmetry in a microorganism is the presence of a cell body and a flagellum. Thus, the force quadrupolar singularity is often associated with the flows produced by flagellated swimmers, e.g., sperm⁹ and bacteria^{14,42,50}. To the best of our knowledge, there have not been any direct experimental measurements of force quadrupolar strengths of flagellated microorganisms. However, numerical simulations are a useful tool for calculating the quadrupolar strengths for varying morphologies. Simulations of model flagellated swimmers show that a longer flagellum and relatively smaller cell body correspond to a positive quadrupole strength, $v > 0$, while a large cell body attached to a shorter flagellum corresponds to a negative quadrupole strength, $v < 0$ ¹⁴. We will see in Section 3.2.3 that the results of our multipole analysis—which

Table 1 The signs of the multipole moments for different microorganisms, estimated based on their propulsion mechanism and morphology. The table entries ‘N.A.’ correspond to multipole moments whose signs can not be ascertained based on our knowledge of their geometries.

Microorganism	κ	σ	v	τ
<i>E. coli</i>	>0	<0	>0	>0
<i>C. reinhardtii</i>	<0	<0	N.A.	≈ 0
<i>Volvox</i>	≈ 0	>0	≈ 0	≈ 0
<i>V. cholera</i>	>0	<0	<0	N.A.
<i>P. aeruginosa</i>	>0	<0	>0	N.A.

considers $v > 0$ (resp. $v < 0$) for long-flagellated (resp. short-flagellated) swimmers—are consistent with the recent simulations by Pimponi *et al.*^{31,43}, thus providing further evidence of this relationship between quadrupole strengths and swimmer morphology. In this way, the sign of the force quadrupole indicates the region of the cell (body plus flagellum) where a greater part of the propulsive thrust or swimming drag is concentrated. Based on some of the observed geometries of bacterial cells, an example of a microorganism with $v > 0$ could be *P. aeruginosa* (cell body length $\approx 1 \mu\text{m}$; flagellar length $\approx 3.4 \mu\text{m}$), while one with $v < 0$ could be *V. cholera* (cell body length $\approx 3 \mu\text{m}$; flagellar length $\approx 2 \mu\text{m}$)^{11,67}. Just like the source dipole for flagellated swimmers, the value of the force quadrupole can be estimated from the scaling $v \sim a^3 V_s$. This is because both the source dipole and the force quadrupole emerge from different variations of the second moment of the stresses exerted by the microorganism on the surrounding fluid⁶⁵, thus they are expected to scale similarly. Finally, the rotlet dipole represents the equal and opposite torques that a helically flagellated microorganism exerts on the fluid^{14,42}. We note here that because we are eventually interested in swimmer distributions transverse to the floating film, we do not discuss the hydrodynamic effects of the rotlet dipole (eqn. 9d) as it does not yield any motion in the \mathbf{e}_3 direction^{14,15,42}.

2.3 Calculation of the hydrodynamic interactions

The ‘ \mathcal{H} ’ terms in eqn. 9, by definition, denote the hydrodynamic influence of the confinement (L-L and A-L) on the swimmer-generated flow. This influence results in the swimmer’s translation and rotation. It is quantified by the Faxén laws for a force-free and torque-free spheroidal particle:

$$\begin{aligned} \mathbf{u}_{HI}(\mathbf{y}, \mathbf{p}) &= \mathbf{u}^{\mathcal{H}}(\mathbf{x} = \mathbf{y}) + O\left(a^2/H^2\right), \\ \boldsymbol{\Omega}_{HI}(\mathbf{y}, \mathbf{p}) &= \left[\frac{1}{2} \nabla \times \mathbf{u}^{\mathcal{H}}(\mathbf{x}) + \frac{\gamma^2 - 1}{\gamma^2 + 1} \mathbf{p} \times \left(\mathbf{E}^{\mathcal{H}}(\mathbf{x}) \cdot \mathbf{p} \right) \right] \Big|_{\mathbf{x}=\mathbf{y}} \\ &\quad + O\left(a^2/H^2\right), \end{aligned} \quad (11)$$

where a/H is the characteristic microorganism size normalized by the height of the film, $\gamma = a/b$ is the aspect ratio of the microorganism and $\mathbf{E}^{\mathcal{H}}$ is the rate-of-strain tensor derived from the

$\mathbf{u}^{\mathcal{H}}$ flow. It is very important to note that in principle, the multipole expansion is a valid description of the flow in the far-field of a swimmer, but remarkably, experiments (see ref.³⁹) and numerical simulations (see ref.¹⁴) have shown that it is accurate up to swimmer-boundary separations as small as one body-length. Also, one could extend the multipole expansion of eqn. 8 even further, but we restrict ourselves to 4 terms for simplicity, and also because these terms capture the essential swimmer dynamics and have easily realizable physical significance. Finally, we note that the only hydrodynamic interactions being considered in our work are that between the swimming microorganisms and the two interfaces. We are neglecting all swimmer-swimmer interactions in our analysis, i.e., we are studying microbial dynamics in the dilute regime.

Along with the hydrodynamics-induced drift and reorientation, a microorganism has its own active motility, can interact sterically with either interface and has a tendency to reorient itself randomly due to structural imperfections. Therefore, the motion of the microorganism is described by the following coupled, non-linear ordinary differential equations:

$$\begin{aligned} \frac{d\mathbf{y}}{dt} &= V_s \mathbf{p} + \mathbf{u}_{HI}(\mathbf{y}, \mathbf{p}) + \mathbf{V}_{st}, \\ d\mathbf{p} &= \{\mathbf{\Omega}_{HI}(\mathbf{y}, \mathbf{p}) \times \mathbf{p} + \mathbf{\Omega}_{RD} \times \mathbf{p}\} dt, \end{aligned} \quad (12)$$

where the ' $\mathbf{\Omega}_{RD}$ ' term corresponds to diffusion induced reorientation of the swimmer with a rotational diffusivity D_r . The expressions for the \mathbf{e}_3 component of $\mathbf{u}_{HI}(\mathbf{y}, \mathbf{p})$, and the \mathbf{e}_2 component of $\mathbf{\Omega}_{HI}(\mathbf{y}, \mathbf{p})$ have been provided, singularity-wise, in the Appendix (see eqns. 33 to 38). These are the only hydrodynamic components responsible for altering the vertical distribution of the swimmers. \mathbf{V}_{st} is the steric-interaction-induced velocity of the microorganism which prevents it from penetrating into the interface; it is implemented as a hard-core repulsion. Finally, note that swimmer elongation will result in steric torques upon contact with the interface, but we neglect them in this study as their influence on the swimmers' spatial distribution is not very significant.

We conclude this section with a physical discussion of the microorganism's behavior within the floating film. The hydrodynamic-interaction-effects will be strongest at swimmer-interface separations corresponding to ~ 1 swimmer body-length^{22,39}; beyond these the swimmer motion will be dictated by self-propulsion and rotary diffusion^{3,40,48}. Thus, in the present configuration, a swimmer near the center of the film is expected to swim toward one of the two interfaces, reach close enough to be affected by hydrodynamic interactions and then translate and/or rotate in a fashion acutely dictated by the type of interface: A-L or L-L, and the morphology of the swimmer: the parameters γ and κ, σ, ν . The near-interface hydrodynamic interactions can lead to various behaviors which we identify, one singularity at a time, in the subsequent sections.

3 Results

3.1 Dimensionless parameters and simulation methodology

We render the equations dimensionless by scaling lengths with the film height H and velocities with the swimming speed V_s . The

key dimensionless parameters in our study are the viscosity ratio, $\lambda = \mu_2/\mu_1$; the swimmer elongation γ ; and the dimensionless force dipole, $\kappa' = \kappa/(H^2 V_s)$; source dipole, $\sigma' = \sigma/(H^3 V_s)$; and force quadrupole, $\nu' = \nu/(H^3 V_s)$ strengths. An inspection of the scaling for the dimensional multipole strengths $\{\kappa, \sigma, \nu\}$ (see Section 2.2) and the non-dimensionalizing scheme employed by us suggests that the dimensionless source dipole and force quadrupole should be an order of magnitude less than the dimensionless force dipole; and this is how we select the parameter values κ', σ' and ν' in our simulations. We note that by definition, higher values of λ correspond to a less viscous fluid-film floating on a more viscous underlying fluid. The symmetry about the azimuthal angle (ϕ) and along the \mathbf{e}_1 and \mathbf{e}_2 directions allows us to study the swimmer motion in terms of only two degrees of freedom: its separation from the L-L, $z' = z/H$, and its orientation $\mathbf{p} = (\cos \theta, 0, \sin \theta)$. Therefore, the swimmers in our simulations are effectively confined to the 2D $\mathbf{e}_1 - \mathbf{e}_3$ plane. We perform probabilistic simulations by integrating eqns. 12 using the explicit Euler method, for $N_b = 1000$ swimmers whose initial positions (resp. orientations) are assigned from a uniformly random distribution between $[a/H, 1-a/H]$ (resp. $[0, 2\pi]$). The simulations run until $t_{end} = 100H/V_s$, after which we extract the probability distribution of the time-averaged swimmer position and orientation, $\Psi(\bar{z}, \bar{\theta})$, where the over-bars denote time-averages:

$$\bar{z} = \frac{1}{t_{end}} \int_0^{t_{end}} \frac{z(t')}{H} dt', \quad \bar{\theta} = \frac{1}{t_{end}} \int_0^{t_{end}} \theta(t') dt'. \quad (13)$$

The distribution function is normalized such that,

$$\frac{1}{2\pi} \int_0^1 \int_0^{2\pi} \Psi(\bar{z}, \bar{\theta}) d\theta d\bar{z} = 1, \quad (14)$$

i.e., $\Psi(\bar{z}_i, \bar{\theta}_j) d\bar{z} d\theta \times N_b/(2\pi)$ yields the number of swimmers within the bin $[\bar{z}_i \pm d\bar{z}, \bar{\theta}_j \pm d\theta]$. Our main objective is to ascertain the time-averaged swimmer distribution as a function of film height, $\mathcal{F}(\bar{z})$, toward which we integrate $\Psi(\bar{z}, \bar{\theta})$ over $\bar{\theta}$, to obtain,

$$\mathcal{F}(\bar{z}) = \frac{1}{2\pi} \int_0^{2\pi} \Psi(\bar{z}, \bar{\theta}) d\bar{\theta}. \quad (15)$$

We also define the 'fraction' of swimmers at the L-L (resp. A-L) as \mathcal{F}^0 (resp. \mathcal{F}^1), given by,

$$\mathcal{F}^0 = \int_0^{1.1\bar{a}} \mathcal{F}(\bar{z}) d\bar{z}, \quad (16a)$$

$$\mathcal{F}^1 = \int_{1-1.1\bar{a}}^1 \mathcal{F}(\bar{z}) d\bar{z}, \quad (16b)$$

where $\bar{a} = a/H$ ⁵⁰. The quantities mentioned above act as useful indicators of the spatial distribution of swimmers as mediated by hydrodynamic interactions, self-propulsion and rotary diffusion.

3.2 Microorganisms in a stagnant, floating film

The major results to be reported in this section are: (i) swimmer distribution in the film, and, (ii) difference in swimmer accumulation at the two interfaces; quantified by: (i) $\mathcal{F}(\bar{z})$, and, (ii) $\Delta\mathcal{F} = \mathcal{F}^0 - \mathcal{F}^1$, respectively. In our simulations we take the films to be relatively thick as compared to the swimmer size, i.e., we have $a/H = 1/50 \ll 1$. As a result, the viscosity ratio is expected to significantly alter the swimming behavior near the L-L, but not near the A-L. Thus for a fixed swimmer geometry, variation in $\mathcal{F}(\bar{z})$ and $\Delta\mathcal{F}$ with respect to the film viscosity (λ) can be explained on the basis of hydrodynamic interactions near the liquid-liquid interface itself. The variation $\mathcal{F}(\bar{z})$ and $\Delta\mathcal{F}$ as a function of the swimmer elongation (γ) however, will require careful consideration of hydrodynamic interactions near both interfaces.

3.2.1 Force dipolar interactions

It is common knowledge that a force dipole is always attracted to nearby interfaces. Hydrodynamic interactions cause pushers (resp. pullers) to orient parallel to (resp. perpendicular to, and ‘facing’ toward) a nearby interface and be attracted to it³⁰. This explains Fig. 2 wherein we have almost exclusive accumulation of swimmers at both the interfaces. There is slightly more accumulation near $\bar{z} \approx 0$ due to nominally stronger hydrodynamic interactions at the liquid-liquid interface. This behavior depends very weakly on both λ and γ , with $\mathcal{F}^0 = \mathcal{F}^1 + \varepsilon$, $\varepsilon \sim O(0.01)$ (see Fig. 16 in Appendix). However, one does see that pullers ($\kappa' < 0$) accumulate closer to both the interfaces than the pushers ($\kappa' > 0$), for all viscosity ratios, λ , and elongations, γ (see additional distributions in Fig. 15 in the Appendix). This is because hydrodynamics causes pullers to orient themselves toward the nearest interface, perpendicular to it; contrary to pushers who orient parallel to the interfaces. In this way the pullers’ motility acts in conjunction with their hydrodynamic attraction to enhance their interface accumulation as compared to pushers. We emphasize here that the stronger attraction of pullers toward a glass surface was recently observed in experiments of *V. alginolyticus*, albeit for swimming speeds larger than $20 \mu\text{m/s}$ ²⁶. In this study, we confirm this effect using just the leading order multipole representation of microorganisms. Thus, dipolar hydrodynamic interactions prove very useful in explaining a salient feature of near surface swimming.

Unlike the distributions in Fig. 2, recent numerical simulations have suggested the existence of significant asymmetry in bacterial propulsion in both thick and thin fluid films resting on a rigid substrates⁴³. This provides us a motivation to study the hydrodynamic interactions resulting from higher order multipoles like the effects of the source dipole and the force quadrupole. We consider these one by one in the subsequent sections to identify key behaviors elicited by each, and comment on their combined effects at the end.

3.2.2 Source dipolar interactions

The flow due to a source dipole is representative of a ‘neutral’ swimmer, i.e., one that is neither a pusher or a puller (as its force dipolar contributions are negligible). The first important point to note about source dipolar interactions is the existence of ‘central

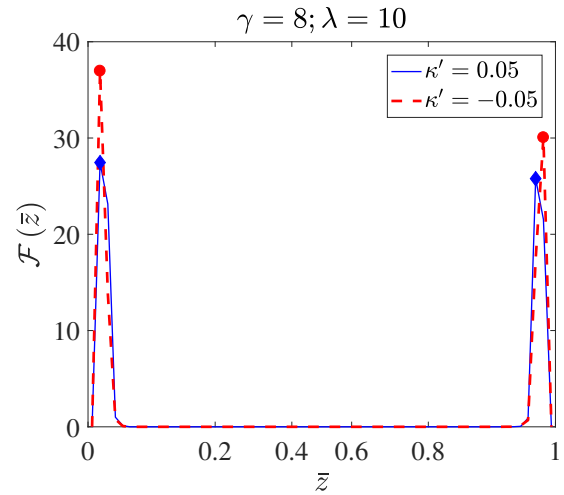


Fig. 2 Swimmer distribution in the film, $\mathcal{F}(\bar{z})$, for $\lambda = 10$ and $\gamma = 8$, for $\kappa' \neq 0, \sigma' = \nu' = 0$. The plots are slightly stretched near $\bar{z} = 0$ and $\bar{z} = 1$, to clearly show the stronger accumulation of pullers near both interfaces. There is not an appreciable difference between accumulation at the two interfaces, with $\Delta\mathcal{F}(\bar{z}) \sim O(0.01)$. These small values of $\Delta\mathcal{F}$ occur for a wide range of swimmer elongation, γ , and the normalized film viscosity λ (see Figs. 15 and 16 in the Appendix). Diamonds (resp. circles) denote maximum values of \mathcal{F} for $\kappa' > 0$ (resp. $\kappa' < 0$). The value of the dimensionless rotational diffusivity of the swimmers is $D_r/(V_s/H) = 0.2$.

oscillations’ for elongated ciliated swimmers ($\sigma' > 0$), as shown in Fig. 3(a-b). It is attributed to the finite-size-effects of the source dipole, which provides a ‘hydrodynamic repulsion’ by turning the swimmer away from any surfaces it is about to encounter. This has been extensively detailed in past studies by Mathijssen *et al.*^{42,65,68}. They demonstrated how this ‘hydrodynamic regularization’ effect causes an elongated source-dipole swimmer to turn away from both a rigid wall and a free surface⁴². They also postulated the use of the source dipole to avoid near-singular flows due to model swimmers near walls⁶⁸. This behavior is also consistent with numerical simulations of model squirmers by Ishimoto and Gaffney¹⁵, wherein they demonstrated the tendency of source-dipole swimmers/neutral squirmers to rotate and swim away from rigid walls as well as free-slip surfaces after reaching a distance of closest approach. The ‘fluidity’ of the interface at $z' = 0$ does not significantly alter this oscillatory behavior. An increase in the viscosity ratio λ increases—ever so slightly—the mean height around which the swimmers oscillate [or, alternatively, the \bar{z} position corresponding to the peak in $\mathcal{F}(\bar{z})$]. This can be seen qualitatively in the sample trajectories of the source dipole swimmers in Fig. 3(c).

A second important concept is the distinctly different spatial distribution for spherical swimmers, depending on the sign of σ' , as seen in Figs. 4(a-b). Ciliated swimmers ($\sigma' > 0$) accumulate near the A-L while non-ciliated swimmers ($\sigma' < 0$) accumulate near the L-L, irrespective of the viscosity ratio. We can get useful insights into this behavior by referring to the deterministic $z'(t) - \theta(t)$ phase portraits of the swimmer dynamics, shown in Fig. 4(c-d). Let us consider the fate of non-diffusing swimmers located initially at the film center, i.e., $z'(0) = 0.5$, and oriented toward

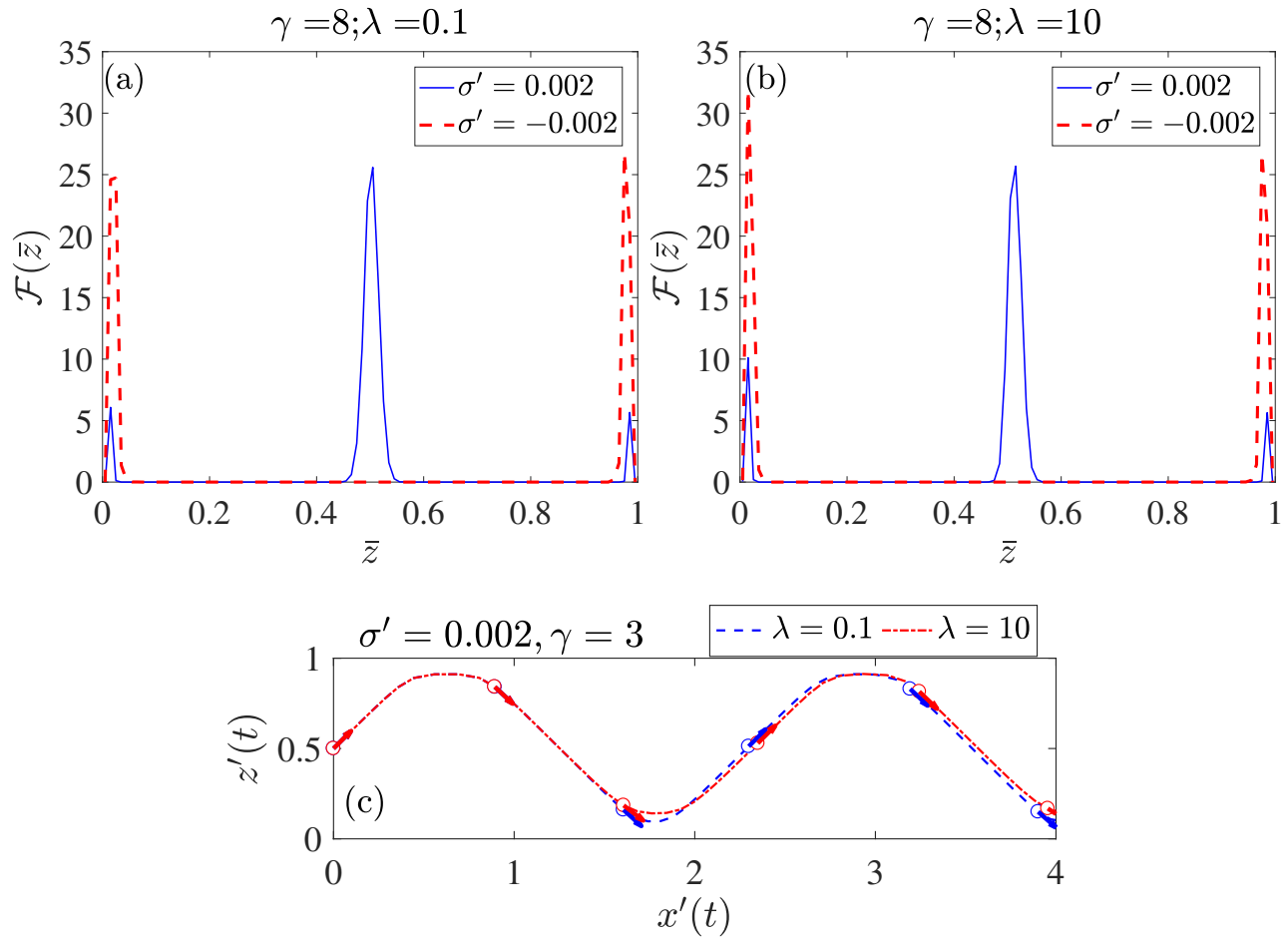


Fig. 3 (a-b) Swimmer distribution in the film, $\mathcal{F}(\bar{z})$, as a function of λ for $\gamma = 8$, for $\sigma' \neq 0$, $\kappa' = \nu' = 0$. (c) Trajectories for a source dipole swimmer with $\sigma' = 0.002$ and $\gamma = 3$. The value of the dimensionless rotational diffusivity of the swimmers is $D_r/(V_s/H) = 0.2$. The trajectories are shown for two different viscosity ratio values, $\lambda = 0.1, 10$. The swimmer orientation \mathbf{p} is shown via the arrows. The initial position of the swimmer is $(x'(0), z'(0)) = (0, 0.5)$, and the initial orientation is, $\theta(0) = \pi/4$.

the L-L, i.e., $\theta(0) > \pi$. Swimmers with a positive source dipolar coefficient (i.e., ciliated swimmers) heading toward the liquid-liquid surface at an angle $\theta(0) = \theta_i > \pi$, are turned away from a minimum-approach height,

$$z'_{\min} \approx \left\{ \frac{\sigma' (4\lambda + 1)}{4 (\lambda + 1)} \right\}^{1/3}. \quad (17)$$

Eqn. 34 in the Appendix shows that z'_{\min} is the height at which the swimmer velocity dz'/dt vanishes, preventing it from descending any further toward the L-L. The swimmer spends some time at this minimum approach height as it reorients and eventually swims toward the free surface. Once near the free surface (A-L), the hydrodynamics-induced angular velocity of a spherical ciliated swimmer vanishes (see second line of eqn. 37) and it can no longer turn away from the A-L. In addition, the vertical component of the swimmer velocity also vanishes at a separation of $(\sigma'/4)^{1/3}$ from the free surface ($\lambda \rightarrow 0$ in eqn. 17; see Fig. 5). Thus, a spherical ciliated swimmer approaching the L-L at an orientation $\theta_i > \pi$ is rotated away from it, swims toward the A-L, gets vertically trapped there and only swims along the length of the film at a fixed orientation θ_f (see trajectories in Fig. 5). This

final orientation of the swimmer is related to the initial orientation, θ_i , as $\theta_f \approx 2\pi - \theta_i$. Note that for $\gamma > 1$ (equivalently, $G > 0$) the A-L can also cause hydrodynamics-induced turning of a ciliated swimmer, leading to the oscillating trajectories discussed in Fig. 3⁴². The time spent by spherical swimmers at a separation of z'_{\min} from the L-L reduces with an increase in the viscosity ratio, λ , as seen qualitatively in Fig. 5. This generalizes past predictions of “an extended residence of the swimmer in the vicinity of the free surface during scattering, compared to a no-slip boundary”¹⁵.

How does inclusion of rotary diffusion affect the above-mentioned deterministic dynamics of ciliated swimmers? It can be seen that introduction of rotary diffusion maintains the tendency to predominantly accumulate near the A-L, except for one important change: some swimmers get permanently ‘trapped’ at the minimum-approach height. This is marked by the local maxima at $\bar{z} = z'_{\min}$ in Figs. 4(a,b). The value of the distribution function at this separation, $\mathcal{F}(\bar{z} = z'_{\min})$, decreases with an increase in the viscosity ratio: from a modest value in Fig. 4(a) to being barely visible in Fig. 4(b) (see also Fig. 17 in the Appendix). This local maximum exists solely because of rotary diffusion. In the deterministic case, the swimmers ‘turn away’ only when θ follows

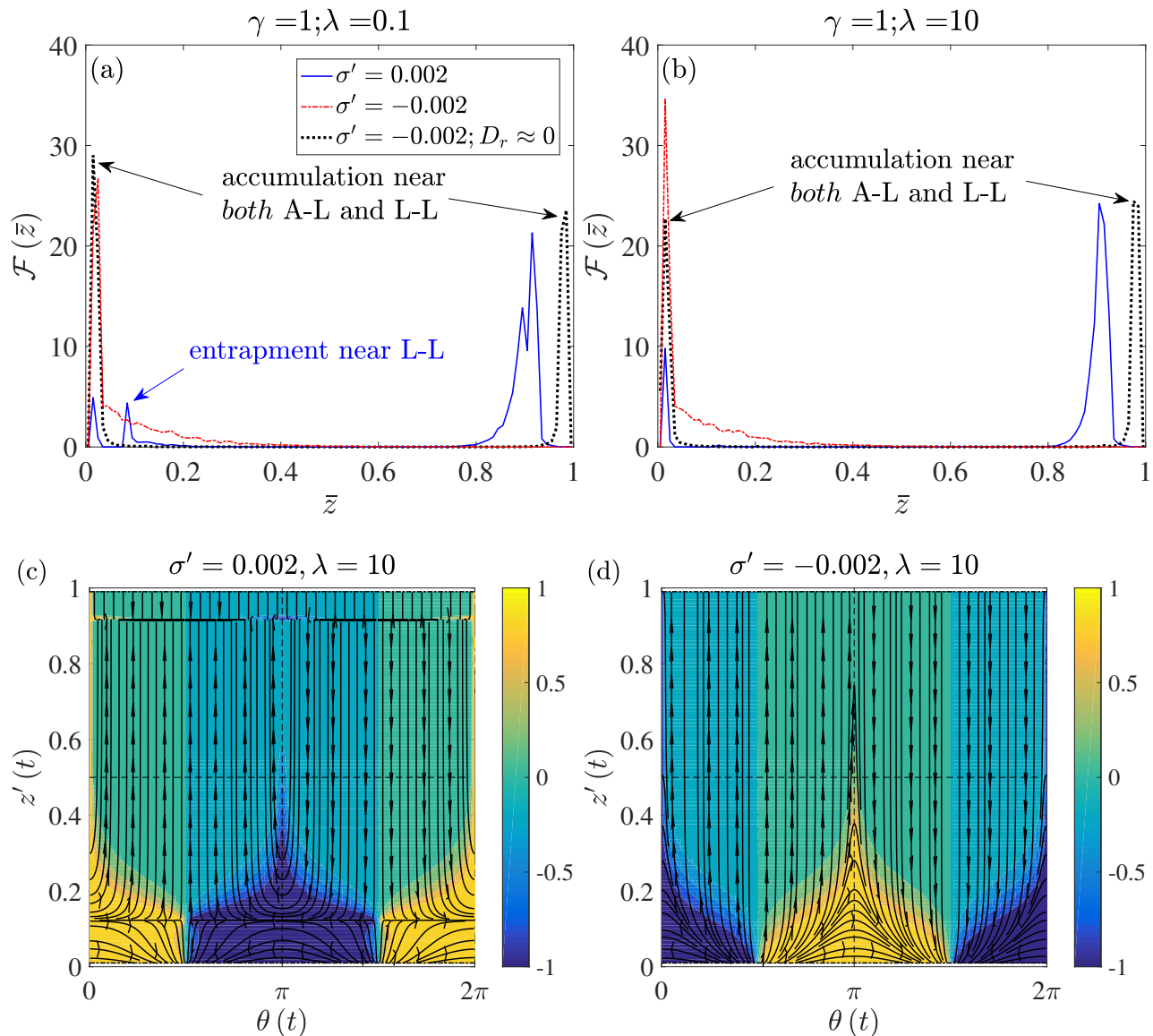


Fig. 4 (a-b) Swimmer distribution in the film, $\mathcal{F}(\bar{z})$, as a function of λ for $\gamma = 1$, for $\sigma' \neq 0, \kappa' = \nu' = 0$. Panel (a) marks a slight peak near $\bar{z} \approx z'_{\min}$, for swimmers with $\sigma' > 0$ (see eqn. 17), by the text 'entrapment near L-L'. This corresponds to the small fraction of swimmers that get perpetually trapped at that height. This peak reduces as λ increases to an extent that it is barely visible for $\lambda = 10$ (see Fig. 17 in Appendix). One can also see how inclusion of rotary diffusion in the dynamics of swimmers with $\sigma' < 0$ (red, dash-dotted lines) causes accumulation *only* at the L-L; while excluding rotary diffusion for these swimmers (black, dotted lines) causes accumulation at *both* at the L-L and the A-L. (c-d) $z' - \theta$ phase planes for spherical swimmers with non-zero source dipoles, demonstrating how/why hydrodynamics in conjunction with rotary diffusion causes, (c) 'top accumulation' for $\sigma' > 0$, and, (d) 'bottom accumulation' for $\sigma' < 0$. The contour represents the normalized angular velocity, $\dot{\theta}/\sqrt{\dot{\theta}^2 + \dot{z}'^2}$, of the swimmer, where dots represent time derivatives. Note that for the ciliated swimmer ($\sigma' > 0$), $\dot{\theta} = -\Omega_{HI}H/V_s \approx 0$ at the distance of closest approach to the A-L ($z' = 1 - (\sigma'/4)^{1/3} \approx 0.92$) and the L-L ($z' = z'_{\min}$; eqn. 17). In all cases with rotary diffusion, the swimmers' rotational diffusivity is taken to be $D_r = 0.2V_s/H$.

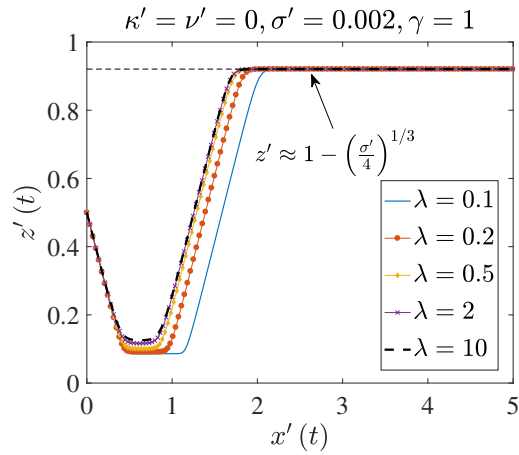


Fig. 5 Deterministic trajectories of spherical source dipole swimmers ($\sigma' > 0, \kappa' = \nu' = 0$) in a floating film with different viscosity ratios λ . It is clear that the time spent by the swimmer close to the L-L decreases as the viscosity ratio increases. After turning away from the L-L the swimmers accumulate at a final height $z'_{final} \approx 1 - (\sigma'/4)^{1/3}$. The swimmers' initial position and orientation are $z'(0) = 0.5$ and $\theta(0) = 7\pi/4$, respectively.

a monotonic reduction from θ_i to θ_f . Rotary diffusion causes θ to change randomly when the swimmer is far from the L-L. This can lead to the swimmers' vertical velocity (dz'/dt) becoming zero *before* they are able to fully turn upward. The swimmers then stay trapped at z'_{min} ; although it must be noted that this trapping is quite different than a fixed point in the $z' - \theta$ phase space, because the swimmers are still free to rotate.

The behavior of non-ciliated swimmers ($\sigma' < 0$) is acutely affected by a combination of hydrodynamic interactions and rotational diffusion. Hydrodynamic interactions alone would cause significant accumulation at both interfaces [thick, dotted line plot in Figs. 4(a,b)], depending on the initial swimmer orientations. Swimmers with $\theta(0) < \pi$ accumulate at the A-L ($z' \approx 1$) without changing their angle of approach, while those with $\theta(0) > \pi$ accumulate at the L-L ($z' \approx 0$) at an angle $3\pi/2$, i.e., pointing toward the L-L. However, as seen in eqn. 37 in the Appendix, the angular velocity ($\mathbf{\Omega}_{HI}^{SD} \cdot \mathbf{e}_2$) vanishes at the A-L for spherical swimmers. So the only source of reorientations at $z' \approx 1$ is rotational diffusion, i.e., the ' $\mathbf{\Omega}_{RD}$ ' term in eqn. 12. This can cause the non-ciliated swimmers at the free surface to eventually point downward, after which they get 'pulled into' the stable attractor in the $z' - \theta$ phase plane [see Fig. 4(d)], leading to accumulation at ($z' \approx 0, \theta = 3\pi/2$). We thus conclude that to accurately estimate the motility of spherical neutral swimmers near a free surface, it is crucial to consider the effects of rotary diffusion in conjunction with hydrodynamic interactions, as the latter alone predict drastically different spatial distributions. In addition to the aforementioned trends of oscillations and asymmetric distributions, we note the small accumulation observed at $\bar{z} \approx 0$ in Figs. 4(a-b), for swimmers with $\sigma' > 0$. This accumulation occurs only for those swimmers whose initial positions lie within $z'(0) < z'_{min} \approx 4a/H$, as is clear from the phase plane in Fig. 4(c). Thus, swimmers within this region cannot escape into the bulk fluid and end up

'colliding' with the liquid-liquid interface. The same effect also explains the minor peaks around $\bar{z} \approx 0, 1$ in Figs. 3(a-b).

3.2.3 Force quadrupolar interactions

The force quadrupolar interactions reveal two fascinating effects which highlight the utility of employing singularity models for microorganisms. The first effect is the preferential accumulation at the free surface for swimmers having larger cell bodies and shorter flagella (i.e., $\nu' < 0$). This is most noticeable for elongated, short-flagellated swimmers in less viscous films (see Fig. 6(d); recall that $\lambda = \mu_2/\mu_1$, and μ_1 is the viscosity of the fluid in which the microorganism swims; so less viscous floating films imply $\lambda > 1$). The asymmetry between accumulation at the free surface versus accumulation at the liquid-liquid interface increases with an increase in both the swimmer elongation and the viscosity ratio. The second important effect revealed by considering force quadrupolar hydrodynamic interactions is the existence of a stable swimming regime near the liquid-liquid interface, for swimmers having long flagella (i.e., for $\nu' > 0$). By stable swimming, we mean a regime wherein the microorganism swims parallel to the liquid-liquid interface at a fixed separation, solely due to hydrodynamic effects. It can be most easily seen in the phase-portraits in Fig. 7(b). The identification of a stable swimming regime from the plots for $\mathcal{F}(\bar{z})$ requires some comment. The spatial distribution plots in Figs. 6(a-c) show a maximum in $\mathcal{F}(\bar{z})$ at either $\bar{z} \approx 0.02$ or at $\bar{z} \approx 0.98$. These maxima correspond to the microorganism being ≈ 1 body length away from either interface, owing to a balance between the hydrodynamics- and motility-based attraction and steric repulsion. It is only for the plot corresponding to $\nu' > 0$ in Fig. 6(d) (blue solid line) that we see a clear maxima at $\bar{z} \approx 0.08$, a separation where the microorganism is not in contact with the liquid-liquid interface and so steric repulsion is absent. Thus, the peak in concentration at $\bar{z} \approx 0.08$ (for $\nu' > 0, \gamma = 8, \lambda = 10$) corresponds to a regime of parallel swimming by long-flagellated microorganisms. Interestingly, this peak corresponding to stable swimming occurs only for slender swimmers in films that are relatively less viscous ($\lambda > 1$).

It is worth noting that numerical simulations of flagellated bacteria swimming in fluid films have also indicated that: (i) bacteria with shorter flagella ($\nu' < 0$ in our model) almost exclusively accumulate at the free surface in thick films, and, (ii) bacteria with longer flagella ($\nu' > 0$ in our model) either accumulate at the free surface, or swim stably at a few body lengths from the wall (see Figs. 4A and 2 in ref.⁴³). These exact behaviors are seen in Fig. 6(d) as well, which is intriguing as we manage to replicate these trends while using a much simpler model for microorganism locomotion. Moreover, our calculations explain that an asymmetry in the propulsive forces exerted by bacteria is at the heart of these varied swimming behaviors. We note here that even though Fig. 6(d) shows the spatial distribution for viscosity ratio $\lambda = 10$, it is not very different from that for $\lambda \rightarrow \infty$. The differences in the accumulation characteristics saturate drastically for $\lambda > 10$ and $\lambda < 0.1$, as will be seen shortly in Fig. 8. In addition to the similarities of stable near surface swimming, we observe the absence of any stable swimming regime near the free surface, for any combination of γ, ν' (notice that all maxima in

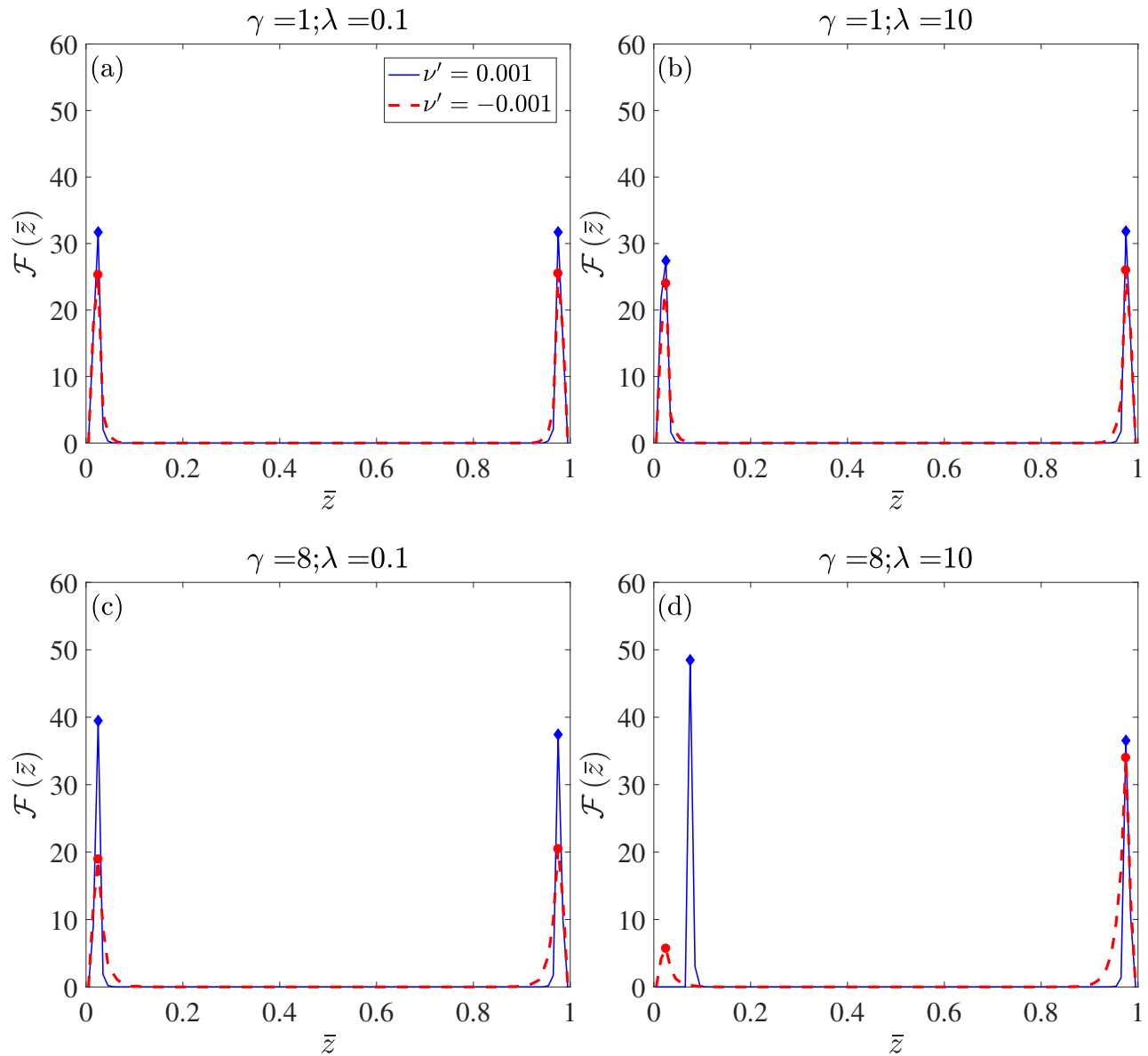


Fig. 6 Swimmer distribution in the film, $\mathcal{F}(\bar{z})$, as a function of λ and γ , for $\nu' \neq 0, \kappa' = \sigma' = 0$. Diamonds (resp. circles) denote maximum values of \mathcal{F} for $\nu' > 0$ (resp. $\nu' < 0$). The value of the dimensionless rotational diffusivity of the swimmers is $D_r/(V_s/H) = 0.2$.

$\mathcal{F}(\bar{z})$ near the free surface occur at $\bar{z} \approx 0.98$). Once again this is in agreement with simulations by Pimponi *et al.* for flagellated swimmers³¹, and by Ishimoto and Gaffney for spheroidal squirmers¹⁵. Additionally, our model is able to accurately predict the stable-swimming-height, say h^* , for the elongated swimmer. In our simulations, h^* is the location of the maximum value of $\mathcal{F}(\bar{z})$, found at $\bar{z} \approx 4a/H = 0.08$ in Fig. 6(d). This value of h^* corresponds to a few swimmer body lengths, and is quite close to that obtained from many other numerical studies for flagellated bacteria swimming near rigid surfaces^{11,38,43}.

While our multipole model very well predicts several phenomena describing dynamics of bacteria near surfaces, there also exist some differences between results of the multipole model and numerical simulations considering bacterial geometries; which does necessitate studies of bacterial propulsion by accounting for de-

tails of their morphology¹¹. One major difference is the nature of bacterial orientation at the stable swimming height h^* : our approach predicts stable swimming of bacteria while they are oriented *toward* the liquid-liquid interface, but simulations reveal that bacteria undergo stable near-surface motion while oriented *away* from the surface. A second important difference between the multipole model and detailed simulations is that the latter reveal the existence of certain initial position-orientation pairs ($z'(0), \theta(0)$) which lead to bacteria with longer flagella ‘colliding’ with nearby rigid walls instead of swimming parallel to them (see ref.⁴³). We would also like to emphasize that simulations predict ‘loss’ of stable swimming when the confinement is increased, i.e., film height is reduced, but our analysis becomes invalid for this particular regime because higher order effects of ‘images of images’ become pronounced for thin films and the ex-

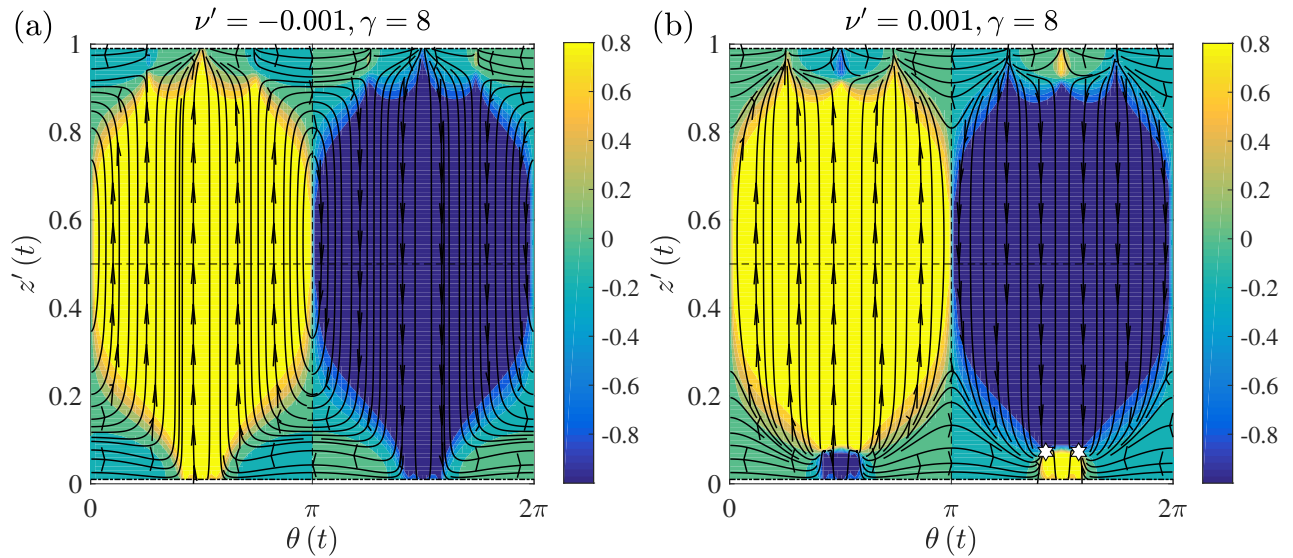


Fig. 7 $z'(t) - \theta(t)$ phase plane for force quadrupole swimmers with (a) $\nu' < 0$ corresponding to microorganisms with relatively shorter flagella, and, (b) $\nu' > 0$ corresponding to microorganisms with longer flagella. The contour represents the normalized translational velocity, $\dot{z}' / \sqrt{\dot{\theta}^2 + \dot{z}'^2}$, of the swimmer, where dots represent time derivatives. In panel (b), the hexagrams at $z' \approx 0.08, \theta \approx 3\pi/2$ show the fixed points near the liquid-liquid interface. These correspond to the stable swimming regime where the microorganism swims parallel to the interface. All other multipole coefficients are set to zero and the viscosity ratio is $\lambda = 10$. The phase plane diagrams for $\lambda \rightarrow \infty$ are quite similar, thus highlighting the similarities in swimming behavior between our reduced-order model and numerical simulations of bacteria with cell body and flagella.

pression for \mathcal{H} used in eqn. 10 loses its applicability. Nevertheless, one can appreciate how multipole models—beyond the force dipole approximation—capture the many dynamical features displayed by microorganisms swimming near rigid and free surfaces.

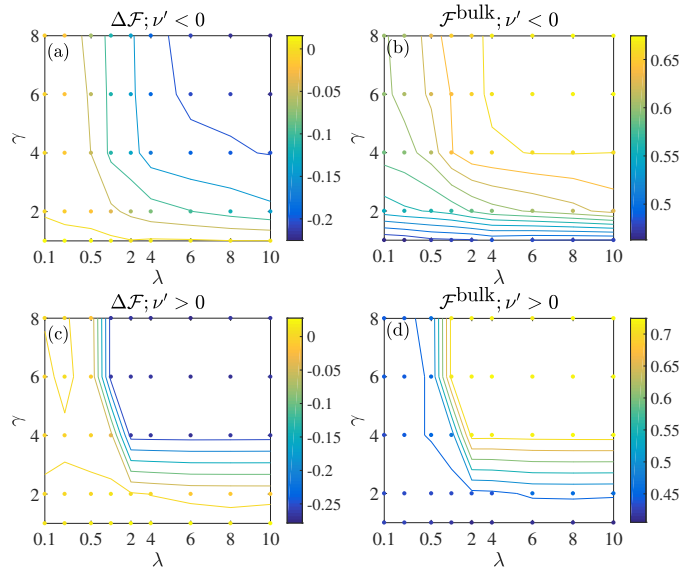


Fig. 8 Summary of boundary accumulation and bulk fraction, as a function of swimmer elongation (γ) and viscosity ratio (λ), for force quadrupole swimmers, i.e., for $\nu' \neq 0, \kappa' = \sigma' = 0$. The horizontal axis is logarithmically spaced (with base 2) until $\lambda = 4$, beyond which it is linear.

Fig. 8 summarizes the distribution characteristics of force quadrupolar swimmers. In Fig. 8(a), for short-flagellated bacteria ($\nu' < 0$), we see that there is monotonic reduction in $\Delta\mathcal{F}$ with

respect to both the viscosity ratio and the swimmer elongation. In the extreme case of elongated bacteria ($\gamma = 8$) residing in films resting on highly viscous substrates ($\lambda = 10$), the number density at the free surface can be $\approx 80\%$ larger than that at the liquid-liquid interface. Fig. 8(c), for long-flagellated bacteria ($\nu' > 0$), also shows that $\Delta\mathcal{F} < 0$ in much of the parameter space but the asymmetry in surface accumulation does not vary substantially; instead there are two regimes of spatial distributions: (i) nearly symmetric swimmer accumulation characterized by $|\Delta\mathcal{F}| \approx 0.05$, and, (ii) no accumulation at the liquid-liquid interface ($\bar{z} \approx 0$) due to stable swimming near it ($\bar{z} \approx 4a/H$), and a more or less constant accumulation at the free surface ($\bar{z} \approx 1$) with $\mathcal{F}^1 \approx 0.2$. The former regime is illustrated by the $\mathcal{F}(\bar{z})$ plots for $\nu' > 0$ in Figs. 6(a-c), while the latter in Fig. 6(d). Fig. 8(c) demonstrates a fine interplay between the aspect ratio of the swimmer and the film's viscosity in ensuring stable swimming near the liquid-liquid interface, as shown by the evident demarcation between data points with $|\Delta\mathcal{F}| \approx 0.05$ and those with $|\Delta\mathcal{F}| \approx 0.20$.

We end this section by discussing another application of the force quadrupolar hydrodynamic interactions: their ability to predict the experimentally observed stable swimming regimes of microorganisms near surfactant-laden free surfaces^{32,69}. While numerical simulations successfully predict the experimentally observed stable swimming of bacteria and spermatozoa near solid walls^{10,11,15}, they fail to do so near free surfaces^{15,31,43}. Experiments on the other hand do reveal that both bacteria (ref.³²) and spermatozoa (ref.⁶⁹) exhibit stable swimming even in the presence of a free surface. The discrepancy between numerics and experiments is attributed to the presence of surfactant molecules—generated by the bacteria, or added artificially—on the air-water interface¹⁵. It is well known that hydrodynamic

interactions of swimmers with surfactant-laden interfaces are markedly different than those for ‘clean’ interfaces^{30,32}. In fact, a free surface covered with an incompressible surfactant having high interfacial viscosity behaves just like a no-slip wall, as far as hydrodynamic interactions are considered^{30,70}. Thus, even though we haven’t modeled surfactant-laden interfaces in our work, our solution in the limit $\lambda \rightarrow \infty$ does correspond to one special case of a surfactant-laden free surface. Consequently, one can expect a fixed point near a surfactant-laden free surface in the $z'(t), \theta(t)$ phase plane of swimmers with long flagella ($v' > 0$), quite unlike the corresponding swimmer dynamics near a clean free surface; the latter being the focus of this work. In this way, a relatively simple multipole expansion up to the quadrupolar term can explain the observations of stable swimming near surfactant-laden free surfaces based on hydrodynamics alone.

3.3 Microorganisms in a flowing, floating film

Thus far, we discussed how hydrodynamics dictates the spatial distribution of model microorganisms within the *stagnant* fluid film of Fig. 1, by separately considering the effects of the fundamental Stokes flow singularities. However, biofilms also exist under flowing conditions and exposure to fluid flow has been proposed as a means to either prevent biofilm formation, or erode biofilms whenever their effects are detrimental. We therefore move our attention to flowing (floating) films in this sub-section, to round up a comprehensive analysis of microbial distribution in interfacial films. The key modifications in the mathematical model from Section 2 are the addition of an external-flow-induced translational ($\mathbf{u}_{ext}^{(1)}$) and rotational ($\mathbf{\Omega}_{ext}$) velocity to the governing equations for swimmer dynamics, i.e., eqns. 12 change to:

$$\frac{d\mathbf{y}}{dt} = V_s \mathbf{p} + \mathbf{u}_{HI}(\mathbf{y}, \mathbf{p}) + \mathbf{u}_{ext}^{(1)}(\mathbf{y}) + \mathbf{V}_{st}, \quad (18)$$

$$d\mathbf{p} = \{\mathbf{\Omega}_{HI}(\mathbf{y}, \mathbf{p}) + \mathbf{\Omega}_{ext}(\mathbf{y}, \mathbf{p}) + \mathbf{\Omega}_{RD}\} \times \mathbf{p} dt,$$

where $\mathbf{u}_{ext}^{(1)}(\mathbf{y})$ is a prescribed velocity profile in fluid-1 [hence the super-script ‘(1)’], evaluated at the position of the microorganism; and,

$$\mathbf{\Omega}_{ext} = \frac{1}{2} \nabla \times \mathbf{u}_{ext}^{(1)}(\mathbf{y}) + \frac{\gamma^2 - 1}{\gamma^2 + 1} \left\{ \mathbf{p} \times \left(\mathbf{E}_{ext}^{(1)}(\mathbf{y}) \cdot \mathbf{p} \right) \right\}. \quad (19)$$

Physically, the external flow ‘carries’ the swimmers along with it; and the velocity gradients in the external flow cause the swimmers to reorient with a rate that balances their tendency to rotate with the local vorticity component (the ‘ $\nabla \times \mathbf{u}_{ext}$ ’ term), and to align with the principal axes of the local extensional flow (the ‘ \mathbf{E}_{ext} ’ term).

We first summarize the influence of external flow on microswimmer motion in a fluid film flowing over a no-slip wall. The external flow in this case is given by the coating-flow profile:

$$\mathbf{u}_{ext}^{(1)}(x_3; \lambda \rightarrow \infty) = v_{max} \frac{x_3}{H} \left(2 - \frac{x_3}{H} \right) \mathbf{e}_1, \quad (20)$$

where v_{max} is the magnitude of fluid velocity at the free surface, and is used henceforth as a measure of the external flow strength.

The dynamics can be viewed under two distinct categories: without and with the consideration of hydrodynamic interactions between swimmers and surfaces. The main result in the first category is that background flow alone can result in different accumulation behaviors of microswimmers in thin films⁵⁰. A strong external flow results in swimmers being carried along the flow while ‘tumbling’ continuously in (near-wall) regions of high shear [red trajectory is Fig. 9(a)]. But for weak external flows, the swimmers spend much more time at the free surface while occasionally ‘dipping’ toward the rigid no-slip surface⁵⁰ [blue trajectory is Fig. 9(a)]. The major results in the second category hint at a competition between reorientation by external flow—abbreviated herein by $\mathbf{\Omega}_{max}$ —and the attractive nature of the force dipolar hydrodynamic interactions—abbreviated by $\mathbf{\Omega}_{HI}$ —resulting in two kinds of behaviors: (i) $\mathbf{\Omega}_{HI} \gg \mathbf{\Omega}_{max}$: the external flow barely affects the swimmer distribution, which are akin to Fig. 2; (ii) $\mathbf{\Omega}_{max} > \mathbf{\Omega}_{max}^{cr} > \mathbf{\Omega}_{HI}$: above a critical flow strength $v_{max}^{cr} \sim \mathbf{\Omega}_{max}^{cr} a$, dipolar swimmers can rotate to get “peeled off” the rigid substrate with their subsequent behavior dictated by the strength of v_{max} . For moderate values of v_{max} (e.g., $v_{max} = 8V_s$), the force dipolar swimmers detach and eventually swim to the A-L [see green trajectory in Fig. 9(b)]. Larger values of v_{max} (e.g., $v_{max} = 20V_s$) significantly delay this rise to the A-L with the swimmers spending an extended amount of time in the high-shear near-wall regions of the flow. This can be seen in the very gradual upward drift for the orange trajectory in the inset of Fig. 9(b). The swimmer trajectories corresponding to these behaviors are shown in Fig. 9. Experimental evidence of fluid shear causing bacterial ‘escape’ from solid surfaces can be found in ref.⁴⁹, while an in-depth discussion of the interplay between motility, external flow and hydrodynamic interactions can be found in refs.^{47,48,50,71}.

In our analysis, we present two important generalizations of the aforementioned results: (i) we discuss the significant differences—both qualitative and quantitative—between flow-induced peeling of spherical pushers and pullers as compared to elongated ones, and, (ii) we quantify the difference in surface accumulation, $\Delta \mathcal{F}$, of pushers and pullers in a flowing, floating film as a function of external flow strength, v_{max}/V_s and viscosity ratio λ . To begin with, we need to obtain an expression for the external fluid flow, and for simplicity we consider a unidirectional flow field. An analytical solution of the form $\mathbf{u}(\mathbf{x}) = u_{ext}(x_3) \mathbf{e}_1$, for the configuration in Fig. 1 with boundary conditions 3, 4 and the ‘decay condition’ $\mathbf{u} \rightarrow \mathbf{0}$ as $x_3 \rightarrow -\infty$, is not straightforward. So we ‘construct’ the following velocity profiles for fluid-1:

$$\frac{\mathbf{u}_{ext}^{(1)}(x_3; \lambda)}{v_{max}} = - \frac{\left[\frac{x_3^2}{2H^2} - \frac{x_3}{H} - \frac{l}{\lambda} (1 + l/2) \right]}{\left[\frac{1}{2} + \frac{l}{\lambda} (1 + l/2) \right]} \mathbf{e}_1, \quad (21)$$

and, for fluid-2:

$$\frac{\mathbf{u}_{ext}^{(2)}(x_3; \lambda)}{v_{max}} = - \frac{\left[\frac{x_3^2}{2H^2} - \frac{x_3}{H} - l(1 + l/2) \right]}{\lambda \left[\frac{1}{2} + \frac{l}{\lambda} (1 + l/2) \right]} \mathbf{e}_1, \quad (22)$$

where the super-scripts ‘(1)’ and ‘(2)’ correspond to the external fluid flow in fluids 1 and 2, respectively. l in eqns. 21 and 22 is

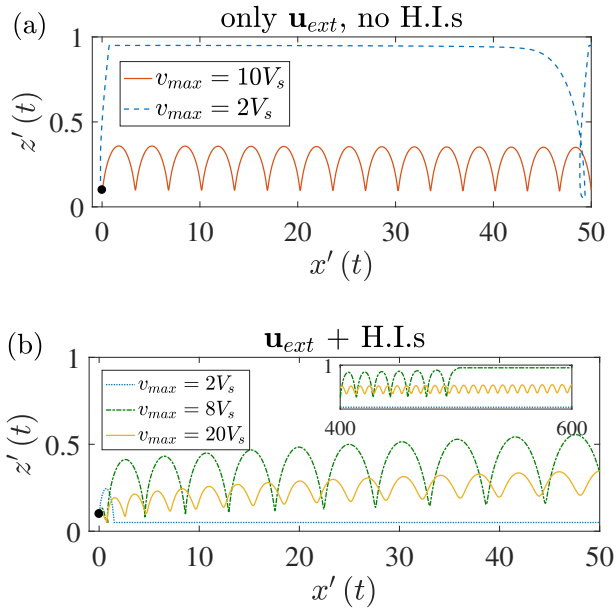


Fig. 9 Swimmer trajectories in a film flowing over a rigid wall, with the external flow given by eqn. 20. (a) Trajectories without inclusion of hydrodynamic interactions (H.I.s), and, (b) trajectories with inclusion of H.I.s for ‘pushers’ with $\kappa' = 6 \times 10^{-3}$. The starting positions and orientations are: (a) $(x'(0), z'(0), \theta(0)) = (0, 0.1, \pi + 0.1)$, and, (b) $(x'(0), z'(0), \theta(0)) = (0, 0.1, \pi/4)$. In panel (a), it is important to note the enhanced time spent at the free surface (resp. near bottom wall) for weaker (resp. stronger) flows. In panel (b) however, this trend is altered due to the inclusion of H.I.s. The inset in panel (b) denotes how the swimmers can escape the rigid wall at $z' = 0$ and be trapped at the free surface at $z' = 1$, under moderate external flow, $v_{max} = 8V_s$. The inset also shows how the swimmers traverse the film centerline in ‘swinging’ trajectories, under strong flows $v_{max} = 20V_s$.

a ‘decay parameter’ whose value is chosen as $l = 5$. This means that the velocity in fluid-2 vanishes at $x_3 = -5H$, i.e., at a distance from the L-L that is five times the thickness of the film. We will comment on the dependence of our results on l at the end of this section. The expression for $\mathbf{\Omega}_{ext}$ is then given by:

$$\mathbf{\Omega}_{ext} = \frac{v_{max}}{H} \frac{(1 - \frac{z}{H}) [1 - G \cos(2\theta)]}{\left[1 + \frac{2l}{\lambda} (1 + l/2)\right]} \mathbf{e}_2, \quad (23)$$

where $G = (\gamma^2 - 1)/(\gamma^2 + 1)$. The velocity profiles given in eqns. 21 and 22 are plotted in Fig. 10 for two values of the viscosity ratio. Eqn. 21 reduces to its corresponding coating-flow expression, eqn. 20, upon taking the limit $\lambda \rightarrow \infty$, as shown in Fig. 10. We now work with the dynamical equations 18 and have a new dimensionless parameter, v_{max}/V_s quantifying the strength of the background flow relative to the swimmer speed in an unbounded, quiescent fluid. In what follows, we only discuss the effects of external flow on the force dipole swimmers, i.e., on pullers ($\kappa' < 0$) and pushers ($\kappa' > 0$). This allows us to use simple physical ideas to explain some of the observed behaviors.

3.3.1 Flow-induced peeling for elongated swimmers

Beyond a critical flow, say $v_{max}^{cr.}$, spherical dipolar swimmers located near a wall and oriented toward it are rotated away from

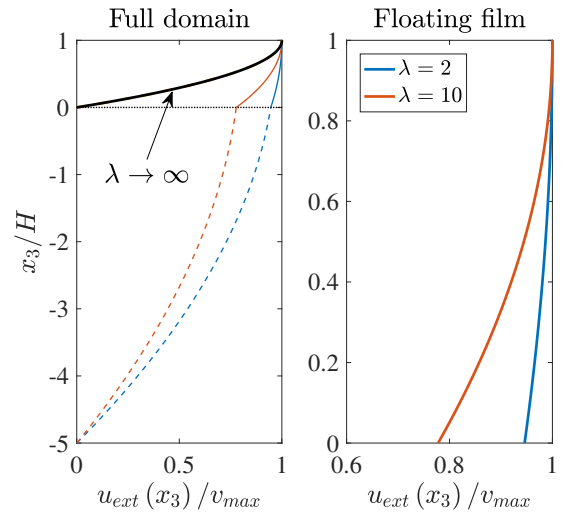


Fig. 10 The velocity profiles given by eqns. 21 and 22 for two different viscosity ratios, $\lambda = 2, 10$. The thick black line is the coating flow profile, eqn. 20, obtained for a film flowing over a rigid wall. A reduction in the shear rate near the L-L with a reduction in λ can be seen clearly.

the wall and get detached to join the bulk flow⁵⁰. In this section, we extend this analysis to the case of spheroidal (elongated) dipolar swimmers and identify an important role of swimmer geometry in their tendency to escape surfaces experiencing strong shear. For the same absolute value of dipole strength, a spherical puller oriented toward the wall requires a larger external flow to be peeled off in comparison to a spherical pusher [see Fig. 11(a)]. The equilibrium orientation for a puller trapped at the wall is $\theta = 3\pi/2$, and so the external flow must work against the hydrodynamic reorientation for a puller, and rotate it by a critical angle $\theta_c^{pull} \approx \pi/2$ before its eventual escape. On the other hand, the equilibrium orientation for a pusher trapped at the wall is $\theta = 0, \pi$. Therefore, even the slightest of external flows causes a pusher pointing toward the wall to rapidly reorient toward $\theta = \pi$. Beyond this, a pusher must rotate by a critical angle θ_c^{push} before it overcomes the hydrodynamic attraction toward the wall and swims away. It can be shown (see ref.⁵⁰) that for spherical dipolar swimmers, $\theta_c^{push} < \theta_c^{pull}$, and so spherical pushers pointing toward the wall require slower external flows to be detached than pullers with the same absolute dipole strength [see Fig. 12(a)]. We have plotted this critical external flow, $v_{max}^{cr.}$, as a function of dipole strength in Fig. 11 along with the results of ref.⁵⁰ for the sake of completeness.

The dynamics becomes considerably more complex for elongated pushers and pullers, due to the rate-of-strain in the external fluid, i.e., the ‘ $\mathbf{E}_{ext}^{(1)}$ ’ term’ in eqns. 23. The critical flow ($v_{max}^{cr.}$) required to detach elongated pullers is now lower than that required for elongated pushers. While the actual value of $v_{max}^{cr.}$ stems from the numerical solution of the non-linear dynamical equations 18, the reasoning behind this can be physically explained based on the nature of the stable orientations of elongated pushers and pullers, and the strength of flow-induced-rotation at these stable orientations: $\mathbf{\Omega}_{ext}$ will be strongest for $\theta = 3\pi/2$ and weakest for $\theta = \pi$. Therefore, even though a spheroidal pusher with

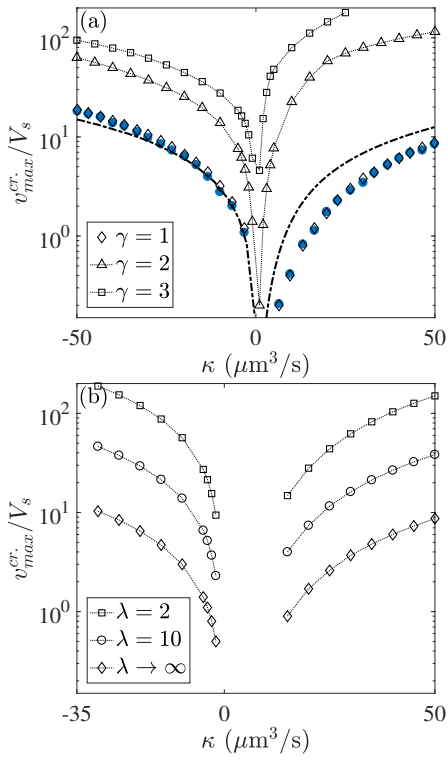


Fig. 11 (a) The minimum/critical external flow required to detach swimmers off a wall, v_{max}^{cr}/V_s , as a function of the swimmer dipole strength, κ , and swimmer elongation γ . Note that v_{max}^{cr} is higher for spherical pullers ($\gamma = 1, \kappa < 0$) than for spherical pushers ($\gamma = 1, \kappa > 0$). v_{max}^{cr} is lower for elongated pullers ($\gamma > 1, \kappa < 0$) than for elongated pushers ($\gamma > 1, \kappa > 0$). The thick dash-dotted lines represent the analytical estimates for the spherical swimmer case, borrowed from ref.⁵⁰ and the blue circles are the results of numerical calculations from ref.⁵⁰. (b) The critical external flow, v_{max}^{cr}/V_s , required to detach *spherical* swimmers off the liquid-liquid interface as a function of the swimmer dipole strength, κ , and the viscosity ratio, λ (which is proportional to the *inverse* of the film viscosity). In both the panels, as mentioned before, $\kappa > 0$ (resp. $\kappa < 0$) denotes pushers (resp. pullers). The swimmers are initially located near the wall at $z'(0) = a/H$ and oriented such that $\theta(0) = 3\pi/2$.

initial orientation $\theta(0) = 3\pi/2$ will quickly reorient to $\theta = \pi$, it will require a much stronger flow in the latter orientation to overcome the hydrodynamic pull, $\mathbf{u}_{HI} \cdot \mathbf{e}_3$, and a stronger hydrodynamic reorientation tendency owing to elongation. A spheroidal puller on the other hand faces stronger ‘overturning’ due to external flow (and steric effects) when it is at $\theta(0) = 3\pi/2$, thus making its reorientation to $\theta = \pi$ relatively easier and requiring lower v_{max}^{cr} than pushers (for same value of $|\kappa|$, of course). These ideas are plotted in Fig. 11(a) and explained schematically in Fig. 12(b).

Fig. 11(b) shows the effect of the ‘fluidity’ of the interface, i.e., the viscosity ratio λ , on the value of v_{max}^{cr} ; wherein we consider the background flow in fluid-1 to be given by eqn. 21. We consider only spherical, dipolar swimmers in the analysis, so Ω_{ext} is a constant for swimmers near the wall and reduces with a reduction in the viscosity ratio (see eqn. 23, but with $z \approx 0, \gamma = 1$). As expected, larger flows are needed for low values of λ because of the reduced flow-shear and the concomitant flow-induced rota-

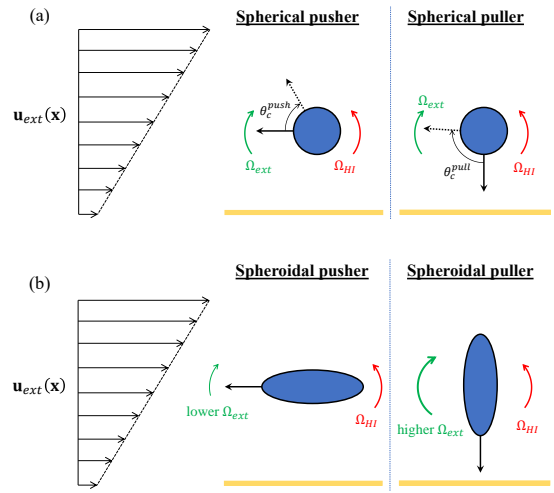


Fig. 12 (a) Schematic depiction of why spherical pushers can escape from a wall at lower values of the critical external flow, v_{max}^{cr} . The dotted arrow represents the orientation at which the pusher/puller can swim away from the wall and escape. The critical angle, θ_c , by which a spherical dipolar swimmer must turn (before it overcomes the wall’s hydrodynamic attraction and swims away) is lower for pushers than for pullers. (b) Schematic depiction of why elongated pullers can escape from a wall at lower values of the critical external flow, v_{max}^{cr} . The angular velocity due to the external flow, Ω_{ext} , is largest when the swimmer is oriented toward the wall, and the angular velocity due to the hydrodynamic interactions, Ω_{HI} , is same for any perturbations to the stable swimmer orientation, i.e., $\theta = 3\pi/2$ (resp. $\theta = \pi$) for a puller (resp. pusher). In this way, pullers face a greater ‘overturning’ effect due to the external flow.

tion (see right panel of Fig. 10). In fact, from the nature of $\mathbf{u}_{ext}^{(1)}$ in eqn. 21 we can understand that the plots for $v_{max}^{cr}/(\Lambda_0 V_s)$ vs. κ , where $\Lambda_0 = \{1 + (l^2 + 2l)/\lambda\}$ will all collapse onto the curve corresponding to $\lambda \rightarrow \infty, \gamma = 1$. One implication of the above discussion is that external flow might not act as an effective means for the removal of biofilms from a liquid-liquid interface, as compared to its efficacy in biofilm erosion off rigid surfaces. Finally we comment on the effect of the parameter l , which signifies a dimensionless ‘decay length’ for the flow field in fluid-2. As evident from eqn. 23, larger values of l result in lower external-flow-induced shear and thus a reduced ability of the external flow to peel swimmers off the L-L, to an extent that for $l > 10$ the external shear becomes so weak that the swimmer detachment from the L-L doesn’t occur even for the largest values of v_{max}/V_s considered in this study.

3.3.2 Spatial distribution of swimmers in a flowing, floating film

Now that we have ascertained the deterministic behavior of force dipolar swimmers in floating, flowing films, we move toward quantifying the swimmer distributions stemming from the randomness in their swimming orientations. We are majorly concerned with the difference in swimmer accumulation at the two interfaces: the quantity $\Delta\mathcal{F} = \mathcal{F}^0 - \mathcal{F}^1$ defined via eqns. 16. More specifically, we investigate how the hydrodynamic flow signature of a swimmer—which could be a pusher or a puller—can affect its statistics in a flowing film. We employ the probabilistic

simulation technique described in the beginning of Section 3 but with the more general eqns. 18, including all physical effects that can influence a microorganism's trajectory.

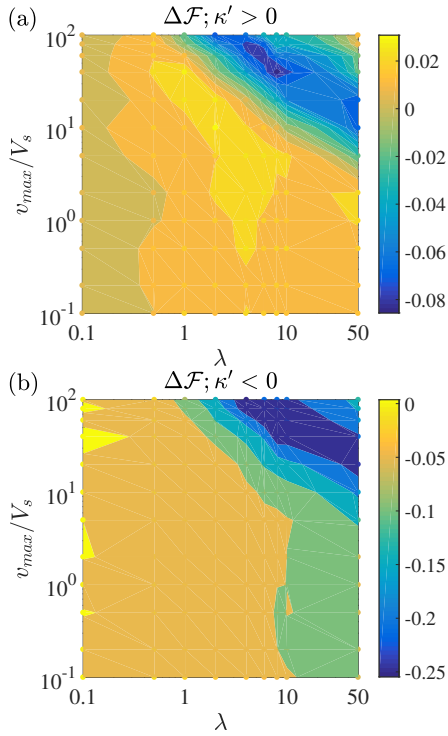


Fig. 13 Contours showing difference between swimmers ‘trapped’ at L-L and A-L for (a) elongated pushers, and, (b) elongated pullers, with $\gamma = 3$. The other parameters are: $|\kappa'| = 0.02$, $\sigma' = \nu' = 0$, $D_r = 0.2V_s/H$.

Figs. 13(a) and (b) reveal a key difference in the film distribution of elongated pushers and pullers. For low shear at the liquid-liquid interface (low values v_{max}/V_s and/or λ) there is a marginally greater accumulation at $z' \approx 0$ for pushers ($0 < \Delta\mathcal{F} < 0.03$), while for pullers the surface accumulation becomes almost symmetric ($10^{-4} < |\Delta\mathcal{F}| < 10^{-3}$). Thus for low shear, pushers show a modest preference toward the L-L, but pullers do not display a strong tendency to accumulate at either interface. As the external flow increases, both pushers and pullers get peeled off the L-L and accumulate more at the A-L, i.e., $\Delta\mathcal{F}$ becomes increasingly negative. As the viscosity ratio λ increases, preferential free-surface accumulation occurs for progressively decreasing values of v_{max}/V_s , owing to stronger shear at the liquid-liquid interface for higher λ values [see eqn. 23, also Fig. 11(b)]. Another important difference between the behavior of pushers and pullers is the extent to which they escape to the free surface, as seen by the $\Delta\mathcal{F}$ values in Figs. 13(a) and (b), respectively. Once swimmer escape from the liquid-liquid interface occurs, the value of $\Delta\mathcal{F}$ is less negative for pushers than for pullers. This is simply a reinterpretation of the higher values of v_{max}^{cr}/V_s for elongated pushers [see Fig. 11(a)]: all other parameters being fixed, external flow of a prescribed strength is always less likely to aid in the escape of an elongated pusher than an elongated puller. A final interesting observation that we make, concerning Fig. 13(a), is the change in the sign of $\Delta\mathcal{F}$ from *negative* to *positive* beyond a certain value

of v_{max}/V_s , seen most clearly for $\lambda = 50$. This is a reflection of the ‘tumbling’ effect that strong external flow has on swimmers, as shown in Fig. 9(b), which results in a high-shear-induced residence of swimmers near the liquid-liquid interface. Note that this effect occurs more easily for elongated pushers than it does for elongated pullers. For elongated pullers, $\Delta\mathcal{F}$ becomes *less negative* for high values of v_{max}/V_s and λ , but it does not become positive like it does for elongated pushers.

4 Discussion and Conclusion

The objective of the current work was to investigate how motility and hydrodynamic interactions influence the spatial distribution of microorganisms in floating fluid films. We approached this problem by utilizing a general multipole-expansion-based singularity model for the swimming microorganisms and quantifying their hydrodynamic interactions with the two interfaces via the ‘method of images’. We then performed probabilistic simulations—with the stochasticity introduced by the swimmers’ rotational diffusion—to obtain statistically significant distributions of the mean swimmer position across the fluid film. The influence of each multipole singularity was explored in isolation and a number of interesting swimming behaviors were observed. An important aspect of our analysis was the generalization of past studies on near-surface swimming. Our simple model yielded many swimming behaviors that were similar to those seen in more complex numerical simulations and in experiments. This highlighted the value of performing a far-field, multipole-expansion analysis of swimming motion. The main results of our work are highlighted in Table 2, and shown pictorially in Fig. 14.

We emphasize here that the result about stable swimming near surfactant-laden free surfaces (for quadrupolar swimmers with $\nu > 0$) did not require an extra set of calculations, and that it can be based solely on our calculations for $\lambda \gg 1$ in Section 3.2.3, and the well-known similarity between incompressible surfactant-laden interfaces and rigid surfaces^{30,70,72}. It is also important to note that even though we studied each singularity in isolation, the behaviors of near-surface stable swimming and preferential accumulation at the free surface (described in Section 3.2.3) are robust to the inclusion of all singularities considered, albeit for certain sets of relative strengths of the singularities. As long as the force quadrupole strength is assumed to be significant, our model gives good qualitative, and somewhat quantitative, agreement with many existing simulations of near-wall/near-free-surface swimming of helically flagellated swimmers^{11,31,38,43}. To the best of our knowledge, existing numerical studies of microswimmer dynamics near non-deforming, *clean* free surfaces have universally predicted the absence of a stable/parallel swimming regime^{15,31}. As a reconciliation with experimental observations, surfactant-induced hydrodynamic effects have been proposed (see ref.¹⁵) as one explanation of the observed parallel swimming regime of flagellated bacteria near free surfaces^{27,32}. If the surfactant effects are modelled as that due to an incompressible surfactant having large interfacial viscosity, then the force quadrupole model can indeed yield a stable swimming regime near *surfactant-laden* free surfaces.

While we performed studies near planar interfaces and com-

Table 2 A summary of the important behaviors elicited by various far-field representations of a microorganism confined in a floating fluid film. The pictorial/schematic representation of these results is shown in Fig. 14.

Multipole	Sign	Physical meaning	Key Behavior
Force dipole (κ)	>0	Propulsion generated behind the cell body, a ‘pusher’	Accumulation at both A-L and L-L, but less tightly than pullers
	<0	Propulsion generated in front of the cell body, a ‘puller’	Accumulation at both A-L and L-L, more tightly than pushers
Source dipole (σ)	>0	Finite sized ciliated microorganism	Preferential accumulation at A-L, ‘entrapment’ near L-L reduces with an increase in the viscosity ratio
	<0	Finite sized flagellated microorganism	Accumulation at L-L (resp. L-L and A-L) when considering (resp. neglecting) rotary diffusion
Force quadrupole (ν)	>0	Relatively longer flagellum (compared to cell body)	Stable swimming near the L-L when the viscosity ratio, $\lambda > 1$; stable swimming near <i>surfactant-laden</i> free surfaces
	<0	Relatively shorter flagellum (compared to cell body)	Preferential accumulation at A-L

pared them to numerical simulations under similar situations, we can also point toward the generality of near-surface motion of bacteria around spherical obstacles. The most important one being that ‘long-tailed bacteria’ get trapped in hydrodynamic bound states around neutrally buoyant, spherical particles; and ‘short-tailed bacteria’ get scattered upon encountering the same spherical particles⁷³. If the spherical particle is large enough in comparison to the swimmer, then, to a first approximation, the analysis of force quadrupolar interactions in Section 3 is able to predict these behaviors as well. We can even go a step further and hypothesize the behavior of flagellated swimmers near neutrally buoyant surfactant-laden drops. As an incompressible surfactant’s ability to cause liquid-liquid interfaces to behave like rigid walls is independent of the viscosity ratio across the interface, we can make a very general observation: as long as a drop is covered by an incompressible surfactant with large enough interfacial viscosity, it will act as a passive hydrodynamic trap for bacteria with long polar flagella, i.e., they can swim along the drop’s surface for substantial times. This can prove to be a particularly useful observation as it will provide an interesting incentive for the use of dispersant in the aftermath of oil-spills, with implications in bacterial bioremediation of heavy oil drops.

The primary motivation of this manuscript was to study microorganism motion in biofilms floating over a base fluid. The spatial distributions discussed in Figs. 3, 4, 6 and 15 tell us how hydrodynamic interactions can affect bacterial concentration in different regions of a film and thus either aid in, or desist from colony formation. However, quite often biofilm formation is accompanied by the bacteria secreting surfactant and other polymeric substances which alter physico-chemistry of their surroundings, most importantly the bulk and interfacial rheology of the fluids involved. In this study, as a first step, we treated the fluids to be Newtonian and the interfaces to be clean but useful extensions can be pursued within the current framework. For example, the effect of interface rheology and more complicated boundary conditions can be probed via the Fourier-transform-based analy-

sis detailed in refs.^{30,74,75}. A useful study in this regard could be drawing equivalence between surfactant-laden interfaces and clean interfaces via identification of ‘effective viscosity ratios’ of the latter, that would help predict swimmer behavior near complex boundaries⁷⁶. The effects of the bulk fluid’s rheology—at least in the weakly non-Newtonian limit—can also be accounted for rather straightforwardly as explained in refs.^{68,77}. A second level of functional detail that can be added to our analysis is the inclusion of active behavior by microorganisms. E.g., many biofilms form over nutrient-emanating substrates and thus chemotaxis—directed motion in search of nutrition^{78,79}—is expected to play an important role in biofilm incipience (see for example, refs.^{80,81}). Chemotaxis could lead bacteria toward the liquid-liquid interface if fluid-2 were to be a nutrient source, or toward the free surface in case of, say, aerotaxis (e.g., for *B. subtilis*)^{82,83}. Yet another form of directed motion, more relevant for algal biofilms, could be positive (resp. negative) phototaxis toward (resp. away from) light sources^{84,85}. The multipole representation would allow one to model a variety of microorganisms (by merely tweaking the multipole strengths in eqns. 9; see Table 1) and the incorporation of active effects would be relatively straightforward in our individual-based model⁸⁶. It would then be an interesting endeavour to see how the more non-trivial hydrodynamic interactions listed in this work interact and compete with bacterial chemotaxis or algal phototaxis to dictate colonization of hot-spots in the numerous scenarios involving films of microorganisms at interfaces^{51,57}.

Conflicts of interest

There are no conflicts to declare.

Acknowledgements

The authors thank the anonymous referees for significantly improving the quality of this manuscript. This research was made possible by grants from the Gulf of Mexico Research Initiative and the National Science Foundation (Grant No. 1700961 and

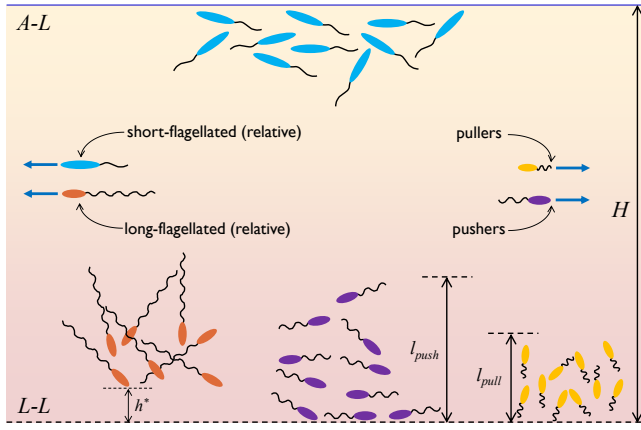


Fig. 14 A schematic of the main results in our problem. $A-L$ (resp. $L-L$) refers to the air-liquid (liquid-liquid) interface. The morphology of the short-flagellated swimmers resembles the bacterium *V. cholera*, while that of the long-flagellated swimmers resembles the bacterium *P. aeruginosa*. These geometries were obtained from ref.⁶⁷. The swimming direction is denoted by the thick blue arrows. Notice that the short-flagellated swimmers ($v' < 0$) accumulate almost exclusively at the $A-L$; while the long-flagellated swimmers ($v' > 0$) accumulate near the $L-L$ at a separation h^* . The difference between pushers ($\kappa' > 0$) and pullers ($\kappa' < 0$) can be understood by noting the flagellar placement relative to the cell body and the direction of swimming, shown by the blue arrows. $l_{pull} < l_{push}$ just denotes that pullers accumulate more tightly near any interface, as compared to pushers. For clarity of the figure, pusher/puller accumulation is shown only near the $L-L$.

1604423).

Appendix

Stokeslet in a floating film: details

A formal solution procedure for our model of swimmer dynamics in a floating film begins with the fundamental solution to the Stokes equations (in fluid-1) perturbed by a point force (called a Stokeslet) at a prescribed position \mathbf{y} :

$$\nabla \cdot \mathbf{u}^{(1)} = 0, \quad (24a)$$

$$\nabla \cdot \mathbf{T}^{(1)} + \mathbf{f}\delta(\mathbf{x} - \mathbf{y}) = \mathbf{0}, \quad (24b)$$

$$\mathbf{u}^{(1)}(|\mathbf{x}| \rightarrow \infty) = \mathbf{0}, \quad (24c)$$

where, $\mathbf{T}^{(1)}$ is the stress tensor in a Newtonian fluid, given by,

$$\mathbf{T}^{(1)} = -P^{(1)}\mathbf{I} + \mu_1 \left(\nabla \mathbf{u}^{(1)} + \nabla \mathbf{u}^{(1),T} \right), \quad (25)$$

with $P^{(1)}$ being the fluid pressure, \mathbf{I} the identity matrix, the superscript ‘T’ denoting transposition and μ_1 is the fluid viscosity. The linearity of the Stokes flow equations allow us to write the solution of eqn. 24 as:

$$\mathbf{u}^{(1)}(\mathbf{x}) = \mathcal{G}^{Os}(\mathbf{x} - \mathbf{y}) \cdot \mathbf{f}, \quad (26)$$

where \mathcal{G}^{Os} is the free-space Green’s function for the problem, the well-known Oseen tensor,

$$\mathcal{G}^{Os}(\mathbf{x} - \mathbf{y}) = \frac{1}{8\pi\mu_1} \left(\frac{\mathbf{I}}{|\mathbf{x} - \mathbf{y}|} + \frac{(\mathbf{x} - \mathbf{y})(\mathbf{x} - \mathbf{y})}{|\mathbf{x} - \mathbf{y}|^3} \right). \quad (27)$$

Now, if instead of being in an unbounded homogeneous fluid-1, the point-force is exerted at a distance z from fluid-2, then one must also solve for the Stoke flow equations in fluid-2 (without the forcing term), subject to the boundary conditions of continuity of velocity and shear stress at the liquid-liquid interface ($L-L$), as given in eqns. 3. This problem (eqns. 24(a,b), 25 and 3) was solved by Aderogba and Blake in ref.⁶². $\mathbf{u}^{(1)}(\mathbf{x})$ can be represented as a superposition of the original force singularity with a system of ‘image singularities’ placed at the ‘image point’ $\mathbf{y}^* = \mathbf{y} - 2(\mathbf{e}_3 \cdot \mathbf{y})\mathbf{e}_3$ (see Fig. 1). One can write

$$\mathbf{u}^{(1)}(\mathbf{x}) = \mathcal{G}^{Os}(\mathbf{x} - \mathbf{y}) \cdot \mathbf{f} + \mathcal{G}_1^{LL}(\mathbf{x}, \mathbf{y}, \mathbf{y}^*; \lambda) \cdot \mathbf{f}, \quad (28)$$

with,

$$\begin{aligned} \mathcal{G}_1^{LL}(\mathbf{x}, \mathbf{y}, \mathbf{y}^*; \lambda) = & -\mathbf{N}^\lambda \cdot \mathcal{G}^{Os}(\mathbf{x} - \mathbf{y}^*) \\ & + \left\{ 2\Lambda_1 z (\mathbf{e}_3 \cdot \nabla_0) + \Lambda_1 z^2 \mathbf{M} \cdot \nabla_0^2 \right\} \mathcal{G}^{Os}(\mathbf{x} - \mathbf{y}^*), \end{aligned} \quad (29)$$

where $\nabla_0 \equiv \partial/\partial\mathbf{y}$, $\mathbf{N}^\lambda \equiv \text{diag.}(\Lambda_2, \Lambda_2, 1)$, with $\Lambda_2 = (\lambda - 1)/(\lambda + 1)$; $\Lambda_1 = \lambda/(\lambda + 1)$; and, $\mathbf{M} \equiv \text{diag.}(1, 1, -1)$. Similarly, the flow-field in fluid-2 can also be represented as contributions from singularities placed at \mathbf{y} , as $\mathbf{u}^{(2)}(\mathbf{x}) = \mathcal{G}_2^{LL}(\mathbf{x}, \mathbf{y}; \lambda) \cdot \mathbf{f}$, with,

$$\begin{aligned} \mathcal{G}_2^{LL}(\mathbf{x}, \mathbf{y}; \lambda) = & \frac{2}{1 + \lambda} \mathbf{R} \cdot \mathcal{G}^{Os}(\mathbf{x} - \mathbf{y}) + \\ & \frac{2}{1 + \lambda} \left\{ z (\mathbf{e}_3 \cdot \nabla_0) - \frac{z^2}{2} \nabla_0^2 \right\} \mathcal{G}^{Os}(\mathbf{x} - \mathbf{y}), \end{aligned} \quad (30)$$

where $\mathbf{R} \equiv \text{diag.}(1, 1, 0)$. Therefore, flow-fields given by $\mathbf{u}^{(1)}(\mathbf{x}) = (\mathcal{G}^{Os} + \mathcal{G}_1^{LL}) \cdot \mathbf{f}$ and $\mathbf{u}^{(2)}(\mathbf{x}) = \mathcal{G}_2^{LL} \cdot \mathbf{f}$ will satisfy the Stokes equations and the boundary conditions in eqns. 3.

One special case of the aforementioned discussion is when the point-force acts near an air-liquid interface ($A-L$). Consider now the presence of an $A-L$ at $x_3 = H$, which requires $\mathbf{u}^{(1)}(\mathbf{x})$ to satisfy the boundary conditions given in eqns. 4, indicative of vanishing normal velocity and shear stresses. The solution to eqns. 24(a,b), 25 and 4 is obtained easily by a slight adjustment and reinterpretation of eqns. 28 and 29. We just need to substitute $\lambda = 0$ in eqn. 29 and note that now the image singularities must lie at $\mathbf{y}^{**} = \mathbf{y} + 2\{H - (\mathbf{e}_3 \cdot \mathbf{y})\}\mathbf{e}_3$ (see Fig. 1). This yields

$$\mathbf{u}^{(1)}(\mathbf{x}) = \mathcal{G}^{Os}(\mathbf{x} - \mathbf{y}) \cdot \mathbf{f} + \mathcal{G}_1^{AL}(\mathbf{x}, \mathbf{y}, \mathbf{y}^{**}) \cdot \mathbf{f}, \quad (31)$$

with,

$$\mathcal{G}_1^{AL}(\mathbf{x}, \mathbf{y}, \mathbf{y}^{**}) = \mathbf{M} \cdot \mathcal{G}^{Os}(\mathbf{x} - \mathbf{y}^{**}), \quad (32)$$

The solutions discussed thus far—for a point force near a $L-L$ or an $A-L$ —are exact in terms of satisfying the governing equations and the appropriate boundary conditions. However, errors are

introduced when *both* these interfaces exist, the configuration of interest in this work. The errors stem from the fact that the fluid velocity in eqn. 28 does not satisfy the boundary conditions given in eqn. 4, and the fluid velocity in eqn. 31 does not satisfy the boundary conditions given in eqn. 3. Therefore, an accurate calculation of $\mathbf{u}^{(1)}(\mathbf{x})$ for a Stokeslet under confinement by two interfaces would require us to obtain successive ‘images of images’ an infinite number of times^{42,59}. However, for the evaluation of a microorganism’s hydrodynamically induced translational and rotational velocities, we can neglect the effect of the higher order images as a first approximation, due to reasons mentioned in Section 2.1.

Hydrodynamically induced linear and angular velocities

The swimmer’s translational velocities, for each of the singularities considered in this work, are:

$$\frac{\mathbf{u}_{HI}^D \cdot \mathbf{e}_3}{V_s} = -\frac{\kappa'(3\lambda+2)}{8(\lambda+1)z'^2} (1-3p_3^2) + \frac{\kappa'}{4(z'-1)^2} (1-3p_3^2), \quad (33)$$

$$\frac{\mathbf{u}_{HI}^{SD} \cdot \mathbf{e}_3}{V_s} = -\frac{\sigma'(4\lambda+1)}{4(\lambda+1)z'^3} p_3 + \frac{\sigma'}{4(z'-1)^3} p_3, \quad (34)$$

and,

$$\frac{\mathbf{u}_{HI}^Q \cdot \mathbf{e}_3}{V_s} = \frac{-v'}{4(\lambda+1)z'^3} \left\{ (9\lambda+6)p_3^2 + (-7\lambda-4) \right\} p_3 + \frac{v'}{2(z'-1)^3} (3p_3^2-2) p_3; \quad (35)$$

while, the swimmer’s rotational velocities are:

$$\frac{\mathbf{\Omega}_{HI}^D \cdot \mathbf{e}_2}{V_s/H} = \frac{3\kappa'}{8z'^3} \left\{ 1 + G \frac{\lambda + (\lambda+2)p_3^2}{2(\lambda+1)} \right\} p_1 p_3 - \frac{3\kappa'}{8(z'-1)^3} (1 + Gp_3^2), \quad (36)$$

$$\frac{\mathbf{\Omega}_{HI}^{SD} \cdot \mathbf{e}_2}{V_s/H} = -\frac{3\sigma'}{8(\lambda+1)z'^4} \left\{ \lambda + \frac{G}{2} (3\lambda+1) (1+p_3^2) \right\} p_1 + G \frac{3\sigma'}{16(z'-1)^4} (1+p_3^2) p_1, \quad (37)$$

and,

$$\frac{\mathbf{\Omega}_{HI}^Q \cdot \mathbf{e}_2}{V_s/H} = \frac{-3v'}{32(\lambda+1)z'^4} \left[\{12\lambda+10\} p_3^2 - 4\lambda - 2 \right] p_1 - \frac{3Gv'}{32(\lambda+1)z'^4} \left[3\{\lambda+2\} p_3^4 - 2p_3^2 - \{11\lambda+4\} \right] p_1 + \frac{3v'}{16(z'-1)^4} \left[\{5p_3^2-1\} + G\{3p_3^4-p_3^2-2\} \right] p_1 \quad (38)$$

The super-scripts ‘D’, ‘SD’ and ‘Q’ in the above equations refer to the force dipole, source dipole and the force quadrupole, respectively. Note that $\mathbf{u}_{HI}^{SD} \cdot \mathbf{e}_3$ in eqn. 34 is proportional to p_3 , just like the swimmer’s self-propulsion in the \mathbf{e}_3 direction, $V_s \mathbf{p} \cdot \mathbf{e}_3$. This allows a source dipolar swimmer’s vertical velocity $(V_s \mathbf{p} + \mathbf{u}_{HI}^{SD}) \cdot \mathbf{e}_3$ to vanish close to the L-L at a distance z'_{\min} (see eqn. 17), thus resulting in the ‘entrapment’ near the L-L as shown in Figs. 4 and 17. As a check for our derivations, we note that taking the limit $\lambda \rightarrow \infty$ in the expressions in eqns. 33 to 38 reduces them to those derived in ref.⁵⁰ for the case of a liquid film (wall at $z' = 0$, free surface at $z' = 1$). For the force quadrupolar expressions, \mathbf{u}_{HI}^Q and $\mathbf{\Omega}_{HI}^Q$, one must multiply our derivations by $-1/2$, because of a different definition of \mathbf{u}^Q (see eqn. 9c), which has also been used in ref.¹⁴.

Accumulation characteristics: additional information

In Section 3.2.1 we had mentioned that pullers accumulate more tightly near both interfaces, irrespective of the values of swimmer elongations, γ , and viscosity ratios, λ . This is shown in Fig. 15 for a further set of values. In addition, we had mentioned that dipolar swimmers do not show a strong preference toward any one interface. Fig. 16 quantifies this statement, showing that the difference in swimmer accumulation at the two interfaces, $\Delta \mathcal{F} = \mathcal{F}^0 - \mathcal{F}^1$ (see eqn. 16), is very small for both pushers and pullers, over a range of values of γ and λ . Figs. 4(a-b) in Section 3.2.2 show the spatial distribution of source dipolar swimmers. In particular, we saw the existence of local maxima near the L-L, at a separation of z'_{\min} given by eqn. 17. This corresponds to the small fraction ($< 10\%$) of swimmers that get trapped at this height. Fig. 17 shows how the value of this maxima reduces as the viscosity ratio, λ , increases. A comparison with the deterministic trajectories of Fig. 5 shows a correlation between a reduction in the swimmers’ retention time and a reduction in the local maximum values of $\mathcal{F}(\bar{z})$, with an increase in the viscosity ratio.

Notes and references

- 1 E. Lauga and T. R. Powers, *Reports on Progress in Physics*, 2009, **72**, 096601.
- 2 J. Elgeti, R. G. Winkler and G. Gompper, *Reports on Progress in Physics*, 2015, **78**, 056601.
- 3 J. Elgeti and G. Gompper, *The European Physical Journal Special Topics*, 2016, **225**, 2333–2352.
- 4 R. M. Harshey, *Annual Review of Microbiology*, 2003, **57**, 249–273.
- 5 A. Karimi, S. Yazdi and A. M. Ardekani, *Biomicrofluidics*, 2013, **7**, 021501.
- 6 M. G. Mazza, *Journal of Physics D: Applied Physics*, 2016, **49**, 203001.
- 7 M. Ramia, D. Tullock and N. Phan-Thien, *Biophysical Journal*, 1993, **65**, 755–778.
- 8 G. Li, L.-K. Tam and J. X. Tang, *Proceedings of the National Academy of Sciences*, 2008, **105**, 18355–18359.
- 9 D. J. Smith and J. R. Blake, *Mathematical Scientist*, 2009, **34**, 74–87.
- 10 D. J. Smith, E. A. Gaffney, J. R. Blake and J. C. Kirkman-

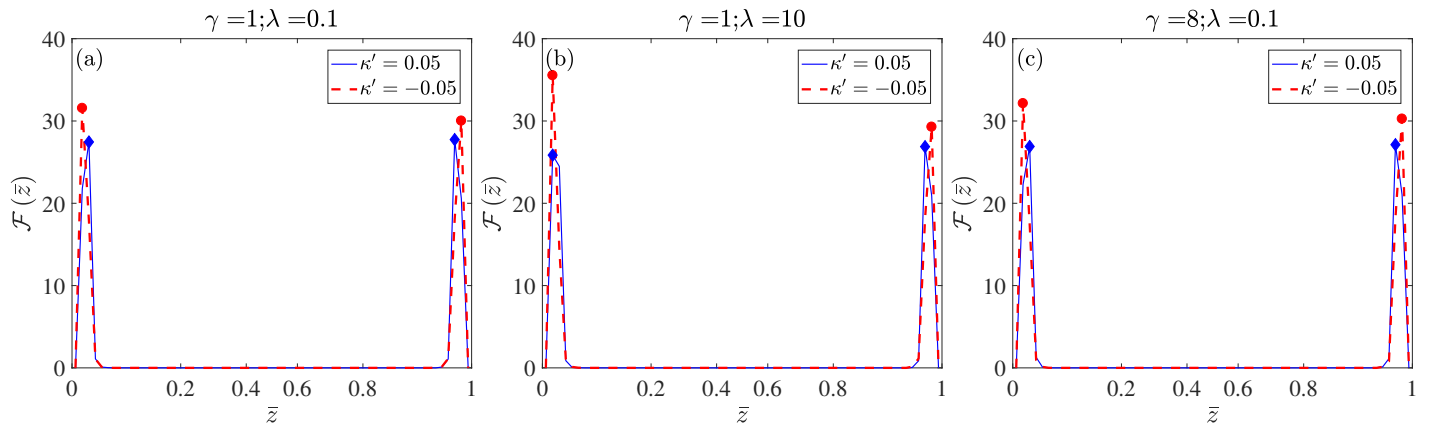


Fig. 15 Swimmer distribution in the film, $\mathcal{F}(\bar{z})$, as a function of λ and γ , for $\kappa' \neq 0, \sigma' = \nu' = 0$. The plots are slightly stretched near $\bar{z} = 0$ and $\bar{z} = 1$, to clearly show the stronger accumulation of pullers near both interfaces. Diamonds (resp. circles) denote maximum values of \mathcal{F} for $\kappa' > 0$ (resp. $\kappa' < 0$); thus showing stronger accumulation of pullers near both interfaces. Notice no appreciable difference between accumulation at the two interfaces, for a wide range of swimmer elongation, γ , and the normalized film viscosity λ . The value of the dimensionless rotational diffusivity of the swimmers is $D_r/(V_s/H) = 0.2$.

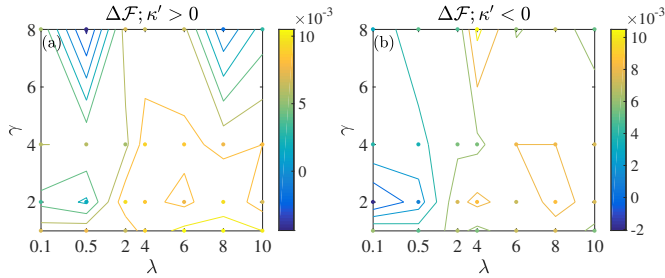


Fig. 16 The difference in interface accumulation $\Delta\mathcal{F}$ (see eqn. 16) for dipolar swimmers: (a) pushers, and, (b) pullers. As discussed in Section 3.2.1, and shown in Figs. 2 and 15, the accumulation when considering only the dipole effects is more or less symmetric with $\Delta\mathcal{F} > 0, \sim O(10^{-3})$.

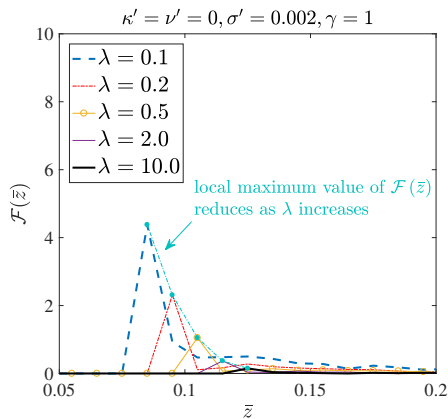


Fig. 17 A magnified view of the distribution function $\mathcal{F}(\bar{z})$ near the L-L for positive source dipolar swimmers, showing the local maxima near the L-L for different viscosity ratios, λ . As described in Section 3.2.2, this maxima stems from the entrapment of the swimmers near the liquid-liquid interface. A reduction in the local maxima as λ increases is apparent.

Brown, *Journal of Fluid Mechanics*, 2009, **621**, 289–320.

11 H. Shum, E. A. Gaffney and D. J. Smith, *Proceedings of the*

Royal Society A: Mathematical, Physical and Engineering Sciences, 2010, **466**, 1725–1748.

12 D. G. Crowdy and Y. Or, *Physical Review E*, 2010, **81**, 036313.

13 D. Crowdy, *International Journal of Non-Linear Mechanics*, 2011, **46**, 577–585.

14 S. E. Spagnolie and E. Lauga, *Journal of Fluid Mechanics*, 2012, **700**, 105–147.

15 K. Ishimoto and E. A. Gaffney, *Physical Review E*, 2013, **88**, 062702.

16 P. D. Frymier, R. M. Ford, H. C. Berg and P. T. Cummings, *Proceedings of the National Academy of Sciences*, 1995, **92**, 6195–6199.

17 P. D. Frymier and R. M. Ford, *AIChE Journal*, 1997, **43**, 1341–1347.

18 M. Vigeant and R. M. Ford, *Appl. Environ. Microbiol.*, 1997, **63**, 3474–3479.

19 M. A.-S. Vigeant, R. M. Ford, M. Wagner and L. K. Tamm, *Applied and Environmental Microbiology*, 2002, **68**, 2794–2801.

20 W. R. DiLuzio, L. Turner, M. Mayer, P. Garstecki, D. B. Weibel, H. C. Berg and G. M. Whitesides, *Nature*, 2005, **435**, 1271–1274.

21 E. Lauga, W. R. DiLuzio, G. M. Whitesides and H. A. Stone, *Biophysical Journal*, 2006, **90**, 400–412.

22 K. Drescher, J. Dunkel, L. H. Cisneros, S. Ganguly and R. E. Goldstein, *Proceedings of the National Academy of Sciences*, 2011, **108**, 10940–10945.

23 G.-J. Li, A. Karimi and A. M. Ardekani, *Rheologica Acta*, 2014, **53**, 911–926.

24 G. Li and A. M. Ardekani, *European Journal of Computational Mechanics*, 2017, **26**, 44–60.

25 S. Bianchi, F. Saglimbeni and R. Di Leonardo, *Physical Review X*, 2017, **7**, 011010.

26 K.-T. Wu, Y.-T. Hsiao and W.-Y. Woon, *Physical Review E*, 2018, **98**, 052407.

27 S. Bianchi, F. Saglimbeni, G. Frangipane, D. Dell’Arciprete and

- R. Di Leonardo, *Soft Matter*, 2019, **15**, 3397–3406.
- 28 B. J. Walker, R. J. Wheeler, K. Ishimoto and E. A. Gaffney, *Journal of Theoretical Biology*, 2019, **462**, 311–320.
- 29 S. Wang and A. M. Ardekani, *Physical Review E*, 2013, **87**, 063010.
- 30 D. Lopez and E. Lauga, *Physics of Fluids*, 2014, **26**, 071902.
- 31 D. Pimponi, M. Chinappi, P. Gualtieri and C. M. Casciola, *Journal of Fluid Mechanics*, 2016, **789**, 514–533.
- 32 L. Lemelle, J.-F. Palierne, E. Chatre and C. Place, *Journal of Bacteriology*, 2010, **192**, 6307–6308.
- 33 R. Di Leonardo, D. Dell’Arciprete, L. Angelani and V. Iebba, *Physical Review Letters*, 2011, **106**, 038101.
- 34 R. Trouilloud, T. S. Yu, A. E. Hosoi and E. Lauga, *Physical Review Letters*, 2008, **101**, 048102.
- 35 D. Crowdy, S. Lee, O. Samson, E. Lauga and A. E. Hosoi, *Journal of Fluid Mechanics*, 2011, **681**, 24–47.
- 36 V. A. Shaik and A. M. Ardekani, *Journal of Fluid Mechanics*, 2017, **824**, 42–73.
- 37 G.-J. Li and A. M. Ardekani, *Physical Review E*, 2014, **90**, 013010.
- 38 H. Shum and E. A. Gaffney, *Physical Review E*, 2015, **91**, 033012.
- 39 A. P. Berke, L. Turner, H. C. Berg and E. Lauga, *Physical Review Letters*, 2008, **101**, 038102.
- 40 G. Li and J. X. Tang, *Physical Review Letters*, 2009, **103**, 078101.
- 41 P. Sartori, E. Chiarello, G. Jayaswal, M. Pierno, G. Mistura, P. Brun, A. Tiribocchi and E. Orlandini, *Physical Review E*, 2018, **97**, 022610.
- 42 A. J. T. M. Mathijssen, A. Doostmohammadi, J. M. Yeomans and T. N. Shendruk, *Journal of Fluid Mechanics*, 2016, **806**, 35–70.
- 43 D. Pimponi, M. Chinappi and P. Gualtieri, *The European Physical Journal E*, 2018, **41**, 28.
- 44 R. Rusconi and R. Stocker, *Current Opinion in Microbiology*, 2015, **25**, 1–8.
- 45 R. Rusconi, J. S. Guasto and R. Stocker, *Nature Physics*, 2014, **10**, 212–217.
- 46 M. T. Barry, R. Rusconi, J. S. Guasto and R. Stocker, *Journal of The Royal Society Interface*, 2015, **12**, 20150791.
- 47 A. Zöttl and H. Stark, *Physical Review Letters*, 2012, **108**, 218104.
- 48 A. Zöttl and H. Stark, *The European Physical Journal E*, 2013, **36**, 4.
- 49 M. Molaei and J. Sheng, *Scientific Reports*, 2016, **6**, 35290.
- 50 A. J. T. M. Mathijssen, A. Doostmohammadi, J. M. Yeomans and T. N. Shendruk, *Journal of The Royal Society Interface*, 2016, **13**, 20150936.
- 51 L. Vaccari, M. Molaei, T. H. Niepa, D. Lee, R. L. Leheny and K. J. Stebe, *Advances in Colloid and Interface Science*, 2017, **247**, 561–572.
- 52 R. M. Atlas and T. C. Hazen, *Environmental Science & Technology*, 2011, **45**, 6709–6715.
- 53 L. S. Dorobantu, A. K. C. Yeung, J. M. Foght and M. R. Gray, *Applied and Environmental Microbiology*, 2004, **70**, 6333–6336.
- 54 H. Abbasnezhad, M. Gray and J. M. Foght, *Applied Microbiology and Biotechnology*, 2011, **92**, 653–675.
- 55 L. Hall-Stoodley and P. Stoodley, *Trends in Microbiology*, 2005, **13**, 7–10.
- 56 R. S. Wotton and T. M. Preston, *BioScience*, 2005, **55**, 137–145.
- 57 J. C. Conrad and R. Poling-Skutvik, *Annual Review of Chemical and Biomolecular Engineering*, 2018, **9**, 175–200.
- 58 J. M. Yeomans, D. O. Pushkin and H. Shum, *The European Physical Journal Special Topics*, 2014, **223**, 1771–1785.
- 59 N. Liron and S. Mochon, *Journal of Engineering Mathematics*, 1976, **10**, 287–303.
- 60 J. R. Blake, *Mathematical Proceedings of the Cambridge Philosophical Society*, 1971, **70**, 303–310.
- 61 J. R. Blake and A. T. Chwang, *Journal of Engineering Mathematics*, 1974, **8**, 23–29.
- 62 K. Aderogba and J. Blake, *Bulletin of the Australian Mathematical Society*, 1978, **18**, 345–356.
- 63 S. Chattopadhyay, R. Moldovan, C. Yeung and X. L. Wu, *Proceedings of the National Academy of Sciences*, 2006, **103**, 13712–13717.
- 64 N. C. Darnton, L. Turner, S. Rojevsky and H. C. Berg, *Journal of Bacteriology*, 2007, **189**, 1756–1764.
- 65 A. J. T. M. Mathijssen, D. O. Pushkin and J. M. Yeomans, *Journal of Fluid Mechanics*, 2015, **773**, 498–519.
- 66 K. Drescher, R. E. Goldstein, N. Michel, M. Polin and I. Tuval, *Physical Review Letters*, 2010, **105**, 168101.
- 67 C. Brennen and H. Winet, *Annual Review of Fluid Mechanics*, 1977, **9**, 339–398.
- 68 A. J. T. M. Mathijssen, T. N. Shendruk, J. M. Yeomans and A. Doostmohammadi, *Physical Review Letters*, 2016, **116**, 028104.
- 69 S. Boryshpolets, J. Cosson, V. Bondarenko, E. Gillies, M. Rodina, B. Dzyuba and O. Linhart, *Theriogenology*, 2013, **79**, 81–86.
- 70 N. Desai, V. A. Shaik and A. M. Ardekani, *Soft Matter*, 2018, **14**, 264–278.
- 71 H. Stark, *The European Physical Journal Special Topics*, 2016, **225**, 2369–2387.
- 72 V. A. Shaik and A. M. Ardekani, *Physical Review Fluids*, 2017, **2**, 113606.
- 73 H. Shum and J. M. Yeomans, *Physical Review Fluids*, 2017, **2**, 113101.
- 74 E. Lauga and T. M. Squires, *Physics of Fluids*, 2005, **17**, 103102.
- 75 A. Ahmadzadegan, S. Wang, P. P. Vlachos and A. M. Ardekani, *Physical Review E*, 2020 (to appear).
- 76 V. A. Shaik and A. M. Ardekani, *Physical Review E*, 2019, **99**, 033101.
- 77 A. M. Ardekani and E. Gore, *Physical Review E*, 2012, **85**, 056309.

- 78 R. Stocker and J. R. Seymour, *Microbiology and Molecular Biology Reviews*, 2012, **76**, 792–812.
- 79 R. Stocker, *Science*, 2012, **338**, 628–633.
- 80 N. Desai and A. M. Ardekani, *Physical Review E*, 2018, **98**, 012419.
- 81 N. Desai, V. A. Shaik and A. M. Ardekani, *Frontiers in Microbiology*, 2019, **10**, year.
- 82 B. L. Taylor, I. B. Zhulin and M. S. Johnson, *Annual Review of Microbiology*, 1999, **53**, 103–128.
- 83 F. Menolascina, R. Rusconi, V. I. Fernandez, S. Smriga, Z. Aminzare, E. D. Sontag and R. Stocker, *npj Systems Biology and Applications*, 2017, **3**, 16036.
- 84 D.-P. Häder and K. Griebenow, *FEMS Microbiology Letters*, 1988, **53**, 159–167.
- 85 A. Giometto, F. Altermatt, A. Maritan, R. Stocker and A. Rinaldo, *Proceedings of the National Academy of Sciences*, 2015, **112**, 7045–7050.
- 86 N. Desai and A. M. Ardekani, *Soft Matter*, 2017, **13**, 6033–6050.

The distribution of microorganisms within a film floating over an underlying liquid depends on their morphology and the viscosity ratio across the liquid-liquid interface.

